International Journal of Sediment Research 33 (2018) 351–370

Contents lists available at ScienceDirect

International Journal of Sediment Research

journal homepage: www.elsevier.com/locate/ijsrc

Original Research

# Flow fields and particle trajectories beneath a tidal bore: A numerical study

Adrien Berchet [a,*], Bruno Simon [b], Anthony Beaudoin [a], Pierre Lubin [b], Germain Rousseaux [a], Serge Huberson [a]

[a] Institut Pprime, SP2MI - Téléport 2, Boulevard Marie et Pierre Curie, BP 30179, 86962 Futuroscope Chasseneuil Cedex, France
[b] Université de Bordeaux, I2M, 16 Avenue Pey Berland, 33607 Pessac cedex, France

ARTICLE INFO

*Article history:*
Received 21 December 2016
Received in revised form
1 September 2017
Accepted 2 March 2018
Available online 8 March 2018

*Keywords:*
Tidal bores
Sediment transport
Trajectories
Physical modeling
Numerical modeling

ABSTRACT

Tidal bores may appear in some estuaries when the tides quickly reach a high level. This phenomenon is rare but has a strong impact during its short duration: i.e. the river bed is significantly eroded and sediments are then transported. In this paper, the trajectories of suspended particles induced by this flow are numerically studied. Four undular bores with Froude numbers between 1.1 and 1.2 are studied. Despite similar Froude numbers, various initial flow conditions were selected to produce or not an inversion of the flow direction during the bore passage. The particle trajectories associated with each distinct flow configuration are presented and analyzed. These trajectories, estimated by solving the Maxey-Riley equation, appear to be very different even though the Froude numbers of flows are similar. These observations are important because the Froude number is often used to characterize a tidal bore as it describes well the free surface, however, it cannot describe the sediment transport. Finally, Chen's model of wave-current interactions is adapted to fit the cases studied and is applied to the four bores simulated. The results highlight that this latter model can reproduce the observed trajectories and dissociate their different components. From this model, it is shown that the inertial and Basset history effects can be neglected compared to the gravity and flow entrainment effects due to the viscous drag when one wants to determine the long-term trajectories of suspended particles.


## 1. Introduction

A tidal bore is a kind of hydraulic jump in translation. If the tidal curve at a given position along a tidal river, namely the water elevation due to the tide as a function of time, is characterized by the presence of an inflexion point, then the tide features a tidal jump (Bonneton et al., 2015; Champion & Corkan, 1936; Rousseaux et al., 2016). As discussed by Bonneton et al. (2012), tidal jumps can be invisible to the eye, but they may be detected by sensors. When they become visible for higher tidal ranges, a tidal jump is then called a tidal bore. In France, tidal bores were formerly called “barres de flot” as in the Seine River because the bore crosses the river section and it happens during the flood phase ("flot") which is much shorter than the ebb phase (“usant”). In the english-speaking countries, the bore comes from the Icelandic "bara" which means a billow or wave. The word appears in the Icelandic proverbial equivalent of the myth Scylla and Charybdis (“sigla milli skers og bàru”, lit. “to sail between a rock and a wave”) (Coates, 2007). In south-western France, near Bordeaux, a tidal bore is called “mascaret” in the local Gascon language, namely the “water rat” because on these rivers with inclined banks, the tidal wave has the appearance of a black rat running fast along the banks. Indeed, a turbid zone (with a dark color due to the turbulence and the mud) is seen on the banks with a jet-like shape similar to the face of a rat (de Lagrave-Sorbie, 1806).

In his seminal study on surges in an open water channel, Favre (1935) distinguished four types of surges (“intumescences”) propagating on the top of the channel current: A- a downstream positive surge (“onde positive d’amont”), B- a downstream negative surge (“onde négative d’amont”), Can upstream negative surge ("onde négative d’aval"), and D- an upstream positive surge ("onde positive d’aval"). A tidal bore is an example of a positive surge propagating upstream. The surge is generated at the head of the tidal wave propagating upstream in a river, the river current being the sum of the current in the river coming from the river source and the current due to the previous tide leaving the river. Other cases of a positive surge propagating upstream can be experienced

* Corresponding author.
*E-mail address:* anthony.beaudoin@univ-poitiers.fr (A. Beaudoin).

https://doi.org/10.1016/j.ijsrc.2018.03.001

either in the laboratory; for example, one produces them, following Bidone (1825), by closing partially or totally a gate in a water channel at the downstream end of the channel: a surge is generated and propagates upstream; one may also produce an analogue of the tidal wave (Rousseaux et al., 2016) or in the field such as a plunging breaker on dissipative beach generates a beach bore in the surf region which propagates upstream in the run-up of the previous breaking wave in the swash zone (Gaughan, 1976). Unfortunately, the term upstream positive surge is somehow incomplete since it does not express if the current in the river is reversed or not due to the passage of the bore. Hence, one should specify if the positive surge propagating upstream induces or not a flow reversal. Indeed, the tidal bore may induce a flow reversal or not, a partial flow reversal in time, a delayed flow reversal (a few minutes after the bore passage), or even a stratified reversal. Partiot (1858) reported a river current reversal close to the bed before seeing a reversal on the free surface using buoys.

In this work, upstream positive surges with or without a flow reversal are studied during the flood phase of the tide (the typical time scale is a few minutes to neglect the temporal evolution of the tide vs. a corresponding time scale of the order of one hour: this hypothesis can be considered as a quasi-static approximation). Conversely, the typical length of stubbles (secondary waves in the undular case) or the bore front (of the order of a few meters) should be small with respect to the longitudinal variations of both the depth and width of the river: this hypothesis can be considered as a quasi-uniform approximation. Therefore, the system (bore+river) will be described by four variables namely $h_1$, $V_1$ for the depth and velocity respectively, on one side of the river and $h_2$, $V_2$ for the depth and velocity respectively, on the other side of the river with respect to the bore front. The velocity vector of the bore, $V_b$, is always opposite to $V_1$ but $V_2$ can initially be either positive or negative with respect to $V_1$. $h_2$ is always higher than $h_1$ in order to have a positive surge. Within this hydrodynamic framework, the sediment transport induced by a tidal bore is studied by an upstream positive surge with or without a flow reversal in the river.

Despite the fact a great deal of work has been devoted to these interactions, the complex phenomenon of sediment transport by a tidal bore still retains an unexplained part for which new insight and new tools may be of some interest. Although at early times interpretations made use of analogies with animals' fights (lobster and eel in the Petitcodiac river (Sentinelles Petitcodiac Riverkeeper [SPR], 2001)), more recent mathematical tools are now available and even a complete Navier-Stokes simulation of bores with simplified geometry is possible (Lubin et al., 2010a; Lubin & Glockner, 2015). However, the velocity and pressure fields do not explain everything and further analysis is still required, especially regarding sediment dynamics. To the best of the authors' knowledge, Chanson and Tan (2011) were the first to tackle the sediment transport locally with the help of experiments. They look to particle trajectories under undular and breaking bores trying to understand the dispersion induced by the flow. An interesting motivation for this work is to assess the spatio-temporal distribution of fish eggs in a tidal bore. This is a subject of current interest for biologists, indeed, the concentration of fish eggs is intimately tied to the salinity along the river and varies during the ebb-flow period (MacInnis, 2012; Reesor, 2012; Tull, 1997). As a matter of fact, biologists have shown that the egg concentration was highest when the salt concentration was lowest. Knowledge of the sediment transport in the water column should be related to the egg concentration in order to better understand the mechanisms associated to the fish reproduction, which is of great environmental interest, especially for endangered species. Chanson and Tan (2011) observed both helicoidal trajectories under an undular bore and chaotic trajectories under a breaking bore. According to them, the orbital trajectories were somehow comparable to the particle motion beneath regular wave crests, but the entire trajectories were a combination of orbital paths superposed to a downstream advection. In the present study, four types of undular bores resulting from the wave-current interaction problem between the river flow and the tidal wave are introduced. It is shown that depending on the flow condition the river current does or does not outweigh the tidal wave even though a tidal bore is observed in both cases. In particular, the different flow configurations are displayed for very close values of the Froude number depending on the tidal bore as well as the river characteristics and conditions using the Computational Fluid Dynamics (CFD) code Thetis. Then, the trajectories of the suspended particles solving the modified Maxey and Riley (1983) equation are presented. From the Chen's model of wave-current interaction (Chen et al., 1964; Chen et al., 2010; Chen et al., 2012; Chen & Chen, 2014; Hsu, 2016), a hydrodynamic analysis is made for the four undular bores considered. Numerical results support the conclusions of this paper.

## 2. Flows studied

### 2.1. Description of the model of positive surges

The first analytical studies of tidal bores were proposed by Barré de Saint Venant (1871) using a quasi-steady flow analogy. Fig. 1 presents a sketch of the classical system used to model tidal bores and surges. For the non-moving frame of reference with respect to the river bottom, $V_1$ is the initial flow velocity positive downstream, $V_2$ is the flow velocity after the bore passage which can be positive or negative depending on the occurrence of the flow reversal or not, $V_b$ is the bore velocity positive upstream. $V_1$ and $V_2$ are considered as the mean flow velocities integrated over the water column. $h_1$ is the initial steady water depth and $h_2$ is the water depth after the bore passage. During its propagation, a bore must satisfy the momentum and continuity principles (Chanson, 2011; Rayleigh, 1908; Stoker, 1957). Neglecting friction losses, assuming a hydrostatic pressure distribution and a constant velocity distribution, the integral form of the equations for the conservation of mass and momentum gives a series of relations between the flow properties during the bore propagation:

$$(V_1+V_2)h_1=(V_2+V_b)h_2, \tag{1}$$

$$g\left(h_2^2-h_1^2\right)=2\quad h_1(V_1+V_b)^2\left(1-\frac{V_2+V_b}{V_1+V_b}\right) \tag{2}$$

where $g$ is the gravitational acceleration. Eqs. (1) and (2) lead to the introduction of a dimensionless number: the Froude number, $Fr$. Within the previous hypotheses, it is defined by:

$$Fr=\frac{V_1+V_b}{\sqrt{gh_1}} \tag{3}$$

which is often used to study tidal bores and surges (Chanson, 2011). In most cases, the Froude number indicates the bore intensity and shape. Four cases are distinguished:

- For a Froude smaller than unity, no bore appears.

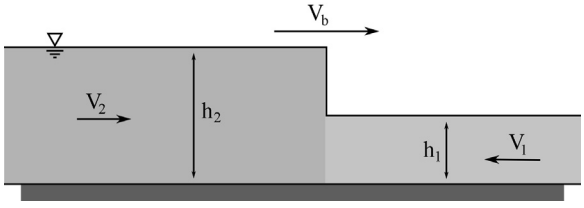


**Fig. 1.** Definition sketch of a surge propagating from the left to the right for an observer standing still within the hypotheses of Eqs. (1) and (2).

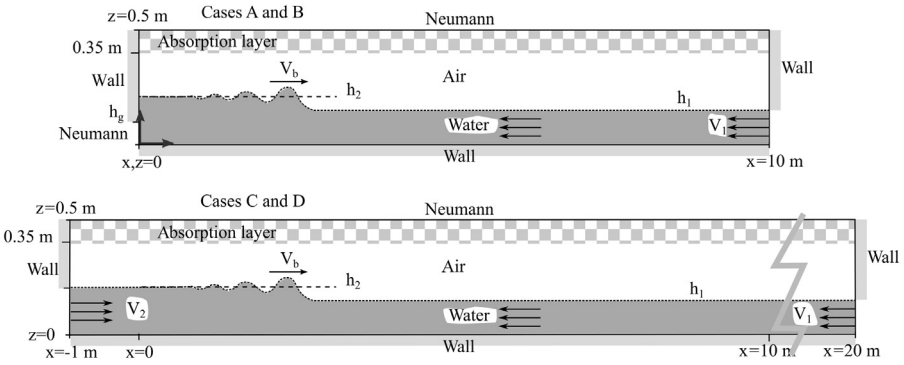


**Fig. 2.** Definition sketch of numerical domains used for the simulations with a bore propagating in the domain.

**Table 1**
Conditions used for the numerical simulations with Froude number $Fr = (V_1 + V_b)/(gh_1)^{0.5}$ and Bore Reynolds number $Re_b = \rho h_1(V_1 + V_b)/\mu$.

| Case | $h_1$ m | $V_1$ m/s | $h_2$ m | $V_2$ m/s | Fr | $Re_b$ | Notes |
|---|---|---|---|---|---|---|---|
| A | 0.165 | −0.23 | 0.199 | 0 | 1.13 | 2.39E+05 | Based on Chanson (2010a) |
| B | 0.1385 | −0.83 | 0.183 | < 0 | 1.17 | 2.02E+05 | Based on Chanson (2010b) |
| C | 0.1 | −0.202 | 0.127 | 0.05 | 1.2 | 1.21E+05 | Solve Eqs. (1) and (2) |
| D | 0.1 | −0.05 | 0.127 | 0.202 | 1.2 | 1.20E+05 | Solve Eqs. (1) and (2) |

- For Froude numbers greater than 1 and less than 1.25–1.5, the bore front consists of a smooth undulation followed by a series of other undulations with decreasing amplitude. The bore is then called an undular bore.
- For Froude numbers greater than 1.5–1.7, a breaking roller appears on the bore front with secondary undulations which are small and hard to distinguish from the breaking roller turbulence. The bore is called a breaking bore.
- The last type, sometimes classified as a breaking or undular bore, has a shape between undular and breaking bores. Its global shape resembles an undular bore but with foaming/breaking of the front and secondary undulations. The Froude number is approximately between 1.25 to 1.6.

Note that this classification is qualitative. Undular bores have been observed for Froude numbers up to 2 (Ryabenko, 1998). Nonetheless, in most cases, the previous classification translates well from field studies into modeled studies, particularly when the effects of bed friction and cross-sectional shape are also taken into consideration (Chanson, 2012).

### 2.2. Presentation of the study cases

The flow hydrodynamics during undular bores was obtained by running four different cases of numerical simulations. All the numerical simulations are two dimensional (2D). Table 1 lists the initial flow conditions used to simulate the bore hydrodynamics with their expected Froude number resulting from the experimental measurements or the analytical formula. Two Cases (A and B) were based on experimental studies in a laboratory channel (Chanson, 2010a, 2010b), whereas the other Cases (C and D) were chosen for their flow conditions being solutions of Eqs. 1 and 2. The latter conditions were selected to model bore conditions where $V_1$ and $V_2$ are in opposite directions contrarily to the cases based on experiments (Table 1). The complete numerical domain consists in a vertical rectangle (Fig. 2) where the bore propagation takes place between $x = 0$ to $x = 10$ m. $x$ is the longitudinal position along the channel, and $z$ is the vertical position above the channel bottom. The domain was filled with water initialized with the depth, $h_1$, and velocity, $V_1$. Depending on the case, $h_1$ and $V_1$ were given by experimental studies or by solving Eqs. 1 and 2. A constant and uniform velocity profile is imposed at the inlet boundary, no attempt being made to match with any velocity profile corresponding to a natural river flow, this being out of the scope of the paper. The study is an idealized 2D numerical exercise showing the different characteristics which can be encountered depending on the boundary conditions. For Cases A and B, the bores were generated by the impact of the flow against a completely or partially closed vertical boundary, similar to the experiments. For Cases C and D, two rectangles of water with different heights, $h_1$ and $h_2$, were set with two flow velocities, $V_1$ and $V_2$, for $x < 0$ and $x > 0$, respectively.

### 2.3. Governing equations and numerical methods

Positive surges were simulated using the CFD code Thetis (Lubin et al., 2010b; Lubin & Glockner, 2015) by solving the Navier-Stokes equations in their multiphase forms (Kataoka, 1986). The governing equations for the Large Eddy Simulation (LES) are classically derived by applying a convolution filter to the unsteady Navier-Stokes equations (Sagaut, 2006). LES models have been developed as a function of the grid size, which can be 2D or three dimensional (3D). So, from a numerical point of view, LES can be used to run 2D or 3D simulations. It has been found that some 2D LES simulations can give very similar results when compared to very fine 3D LES simulations for some averaged quantities such as the energy dissipation (Lubin & Glockner, 2015; Marques Rosas Fernandes et al., 2016). As the Reynolds number is around 100,000 (based on a typical depth of the water, i.e. half a meter), the flow is turbulent which validates the use of a LES model. The interface air/water was tracked by a Volume Of Fluid method (VOF) using a piecewise linear interface construction model (Youngs, 1982). The system of equations yields:

$$\nabla \cdot u = 0, \tag{4}$$

$$\rho\left(\frac{\partial u}{\partial t} + (u\bullet\nabla)u\right) = \rho g - \nabla p - B_u - \frac{\mu}{K}u + \nabla \cdot \left[(\mu+\mu_t)(\nabla u + \nabla^T u)\right], \tag{5}$$

$$\frac{\partial C}{\partial t} + u \cdot \nabla C = 0 \tag{6}$$

where $\mathbf{u}(x,z,t)$ is the actual velocity at a point $(x,z)$ and a time $t$, $\rho(x,z,t)$ is the fluid density, $p(x,z,t)$ is the pressure, $Bu$ is a matrix penalizing the velocity components on the boundary, $\mu(x,z,t)$ is the fluid viscosity, $K$ is a permeability coefficient, $\mu_t$ is the turbulent viscosity, and $C(x,z,t)$ is the phase function. These two latest quantities enable the setting of an absorption boundary condition at the upper limit of 2D numerical domains, as discussed in the next section. The turbulent viscosity, $\mu_t = \nu_t\rho$ where $\nu_t$ is the Kinematic turbulent viscosity, is calculated with the Mixed Scale model (Sagaut, 2006). It is derived from a weighted geometric average of the Smagorinsky (1963) subgrid scale model and the Turbulent Kinetic Energy (TKE) subgrid scale model (Bardina et al., 1980) ($\nu_t = (\nu_{t,smago})^{0.5}\text{-}(\nu_{t,TKE})^{0.5}$). The magnitude of physical characteristics of fluids depends on the local phase. The physical characteristics are defined according to $C$ as:

$$\rho = C\rho_w + (1-C)\rho_a \text{ and } \mu = C\mu_w + (1-C)\mu_a \quad (7)$$

where $\rho_a$, $\rho_w$, $\mu_a$, and $\mu_w$ are the densities and viscosities of air and water, respectively. Time discretization of the momentum equation is implicit and an Euler scheme is used. The velocity/pressure coupling under the incompressible flow constraint is solved with the time splitting pressure correction method (Goda, 1979). The equations are discretized on a staggered grid by means of the finite volume method. The space derivatives of the inertial term are discretized by a hybrid upwind-centered scheme, whereas the viscous term is approximated by a second order centered scheme. The interface tracking is achieved by a VOF method and a Piecewise Linear Interface Calculation (PLIC) (Youngs, 1982). This method has the advantage of building a sharp interface between the air and the water.

A phase function, $C$, is used to locate the different fluids. Since the phase function is not defined at each point where the viscosities and densities are needed for the Navier-Stokes discretization, the physical characteristics are interpolated on the staggered grid. Linear interpolation is used to calculate the density on the velocity nodes, whereas harmonic interpolation is used for the viscosity. The Message Passing Interface (MPI) library is used to parallelize the code, the mesh being partitioned into equal size subdomains to ensure load balancing. The HYPRE parallel solver and preconditioner library is used to solve the linear systems (Falgout et al., 2006). The numerical code has already been extensively verified and validated through numerous test-cases including mesh refinement analysis for coastal applications (Lubin et al., 2006, 2010a, 2010b; Lubin & Glockner, 2015; Simon, 2013). The accuracy of numerical schemes and the conservation laws of mass and energy in the computational domain have been accurately verified.

### 2.4. Initial conditions of the numerical simulations

Two-dimensional numerical domains were used in this study and partitioned into 32 subdomains (one processor per subdomain). For Cases A and B, the bore propagates in a domain similar to experimental conditions (Fig. 2). For Cases C and D, there is no experimental measurement where $V_1$ and $V_2$ are in opposite directions, therefore, the domains needed to be longer than for Cases A and B (Fig. 2). It was necessary for the simulation initialization as well as to increase the duration of the bore propagation in order to track the sediment particles during the complete bore passage.

In each case, the domain was 0.5 m high to avoid water from leaving the numerical domain through the top boundary during the splash happening when the flow runs up the downstream boundary. The water and the air filled the domain (Fig. 2). The viscosities of air and water were set to $\mu_a = 1.85 \times 10^{-5}$ kg/m s and $\mu w = 10^{-3}$ kg/m s, respectively, and the densities of air and water were set to $\rho_a = 1.176{,}8$ kg/m$^3$ and $\rho_w = 1000$ kg/m$^3$, respectively, under a gravity of 9.80 m/s$^2$. The channel bed was set with a no-slip boundary. The channel inflow (right side) continuously injected water between $z = 0$ and $h_1$ at a velocity $V_1$ for every simulation. This is done to satisfy Eqs. (1) and (2) on the right-hand side of the bore (Fig. 2) with the two components of the flow velocity, longitudinal $u_x = V_1$ and vertical $u_z = 0$ m/s, on the right boundary. The top of the domain was set with a Neumann condition letting the air move freely in and out of the domain. Such a condition can induce non-physical velocities. This potential error was controlled using an absorption layer. The absorption layer was a 0.15 $m$ zone located beneath the top boundary with a smaller permeability than the air set to $K = 10^{-5}$ m$^2$.

For Cases A and B, the 2D numerical domains are discretized into 5500 × 500 regular Cartesian cells. The grid is evenly distributed in longitudinal and vertical directions, giving a mesh grid resolution of $\Delta x = 2 \times 10^{-3}$ m and $\Delta z = 10^{-4}$ m. In order to generate the bore for Cases A and B, the outflow boundary was closed between $z = h_g$ to 0.5 m with a no-slip boundary keeping a Neumann condition between $z = 0$ m to $hg$ where $h_g$ is the opening of the gate.

For Cases C and D, the 2D numerical domains are discretized into 7500 × 500 non-regular Cartesian cells. In the longitudinal direction, the grid is clustered with a constant grid size $\Delta x = 2 \times 10^{-3}$ m below $z = 3 \times 10^{-2}$ m from $x = -1$ m to $x = 10$ m, then increasing exponentially for $x > 10$ m. In the vertical direction, the smallest mesh grid resolution $\Delta z_{min} = 5 \times 10^{-5}$ m is set at the bottom, then the grid is clustered with a constant grid size $\Delta z = 5 \times 10^{-4}$ $m$ in the free-surface region. A non-regular grid resolution is used here, with a maximum mesh grid size at the top of the numerical domain. The water was injected in the domain ($x = -1$ m) at a velocity $V_2$ between $z = 0$ to $h_2$ ($u_x = V_2$ and $u_z = 0$ m/s on this part of the boundary).

For both simulations, the rest of the inflow conditions were set with a no-slip boundary. The details of the computational properties are listed in Table 2.

## 3. Flow hydrodynamic properties

### 3.1. Case A: hydrodynamics dominated by undulations

Case A started with the downstream boundary completely closed, $h_g = 0\,m$. The flow impacted the gate without splash but created an elevation of the water level propagating upstream. Fig. 3 shows the dimensionless time evolution of the free surface at two locations from the gate, comparing numerical data and experimental measurements. The 2D numerical simulation reproduced the free surface evolution with good agreement. A direct comparison (the ratio of the numerical results over the experimental data) showed that the bore conjugated depth, the first undulation maximum height and the first undulation minimum depth were within 2% of the experimental data (Chanson, 2010a). The wavelength and amplitude were simulated within 9% of the experimental data, while the bore celerity was found to be within 1% error. Fig. 3 shows the velocity signals measured at $x = 7.15$ m away from the gate and $z = 0.065{,}8$ m deep. Both

**Table 2**
Details of domain meshes (Mesh), processor numbers (Proc), iteration numbers (Iter), Central Processing Unit time (CPU) and Real time (Time) for the simulations.

| Case | Mesh | Proc | Iter | CPU (h) | Time (s) |
|---|---|---|---|---|---|
| A | 5000 × 500 | 32 | 30,000 | 4400 | 9 |
| B | 5000 × 500 | 32 | 440,000 | 9500 | 15.1 |
| C | 7500 × 500 | 32 | 22,300 | 360 | 20.1 |
| D | 7500 × 500 | 32 | 22,600 | 540 | 18.2 |

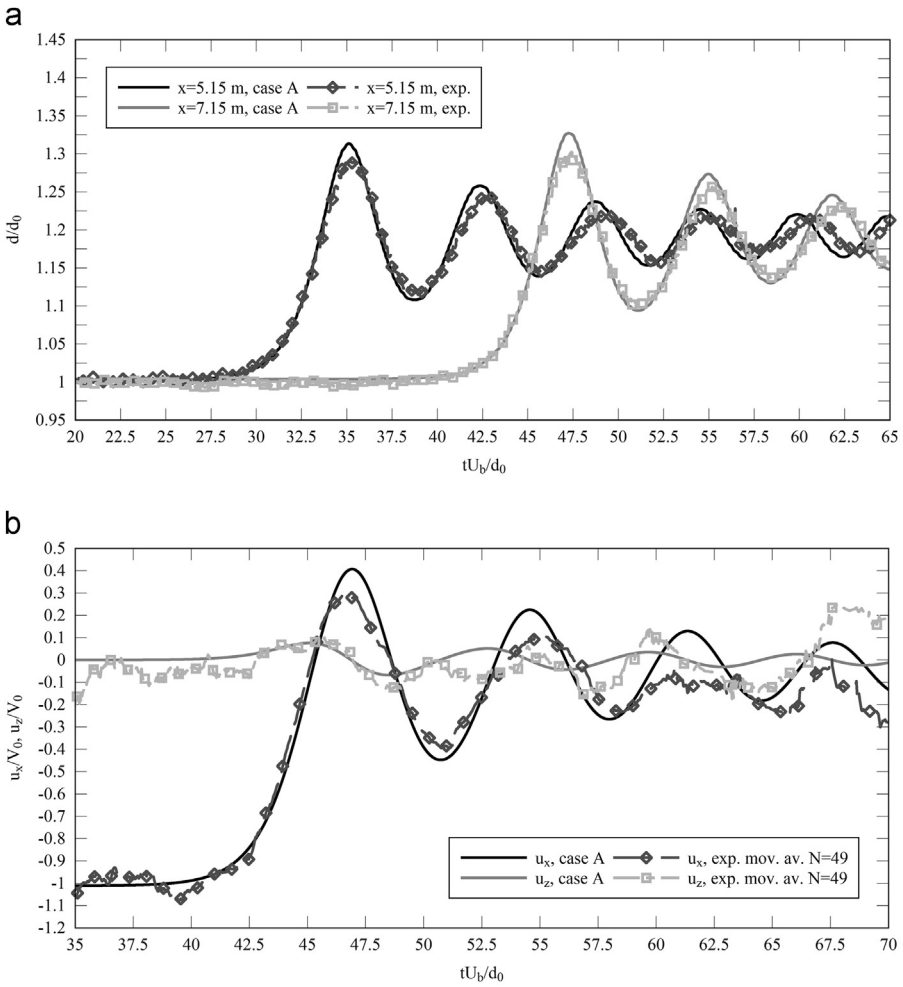


**Fig. 3.** Comparison between numerical simulations and experimental (exp) data. Top figure: time evolution of the free surface $d/d_0$ of undular bores where $d_0$ is the initial water depth. Bottom figure: time evolution of horizontal and vertical components of the flow velocity, $u_x/V_0$ and $u_z/V_0$, at $z/d_0 = 0.18$ with $V_0$ the initial velocity (where mov. av. = moving average and N = number of measured data).

velocity components are compared to the experimental measurements, showing similar trends and evolutions as the bore propagates.

Fig. 4 shows the variation of the velocity magnitude $\|\mathbf{u}\|$ during the bore propagation (Case A) at three different times with streamlines and black isolines of $u_x = 0$ m/s. Within the first meter of propagation, the bore quickly took the form of an undular bore followed by secondary undulations (Fig. 4). As the bore propagated, the front amplitude increased, while smaller undulations appeared one after another at the wave train tail. The amplitude and wavelength of the secondary undulations decreased from the bore front towards the tail (Fig. 4). Between the tail of the wave train and the gate ($x = 0$ m), the water level remained mostly unchanged for the entire bore propagation. The reached water level was equal to the bore conjugate depth, $h_2$.

Looking now at the flow velocity evolution, it evolved in synchronization with the free surface motion (Fig. 4). The longitudinal component, $u_x$, of the flow velocity was completely positive and mostly negative beneath the crest and the trough, respectively, as shown by the streamlines in Fig. 4. Beneath the first crest, the longitudinal component of the flow velocity changed direction flowing upstream along the entire water column (contour line in Fig. 4). Under the front and close to the bed, the flow reversal was particularly strong with an intensity of $1.1 \times V_1$ at $z = 2$ mm above the bed. Beneath the first wave trough, the flow direction changed again, flowing downstream except on a small zone near $z = 0$ m. This zone was detached from the bed and located between $z \approx 1$ to 3 mm. As a consequence, a zone of the flow velocity reversal was observed close to the bed.

Beneath the following secondary undulations, the longitudinal component of the flow velocity followed a similar pattern to the one observed beneath the first wave crest and the trough with a longitudinal component of the flow velocity flowing alternatively upstream and downstream but with a velocity range progressively decreasing (Fig. 4). Nonetheless, after the second or third wave trough, the longitudinal component of the flow velocity was oriented upstream a few millimeters beneath the free surface of the wave troughs (isoline $u_x = 0$ m/s in Fig. 4). For this case, the flow mostly changed direction beneath each wave crest and trough. Moreover, the flow velocity was nearly zero after the bore passage, between the wave train tail and the gate. It was expected to be zero for the bore flow parameters to be the solution of Eqs. 1 and 2. A more detailed analysis was presented in Simon (2013). Here, the flow was dominated by the undulations (Berchet, 2014).

### 3.2. Case B: hydrodynamics dominated by the initial current

Case B started with the downstream boundary partially closed ($h_g = 0.1$ m). As the flow impacted the gate, splashing occurred with some air bubbles entrained below the gate. The water accumulating against the gate remained chaotic and bubbly during the first meter of propagation (Fig. 5). Then, the unsteady free surface

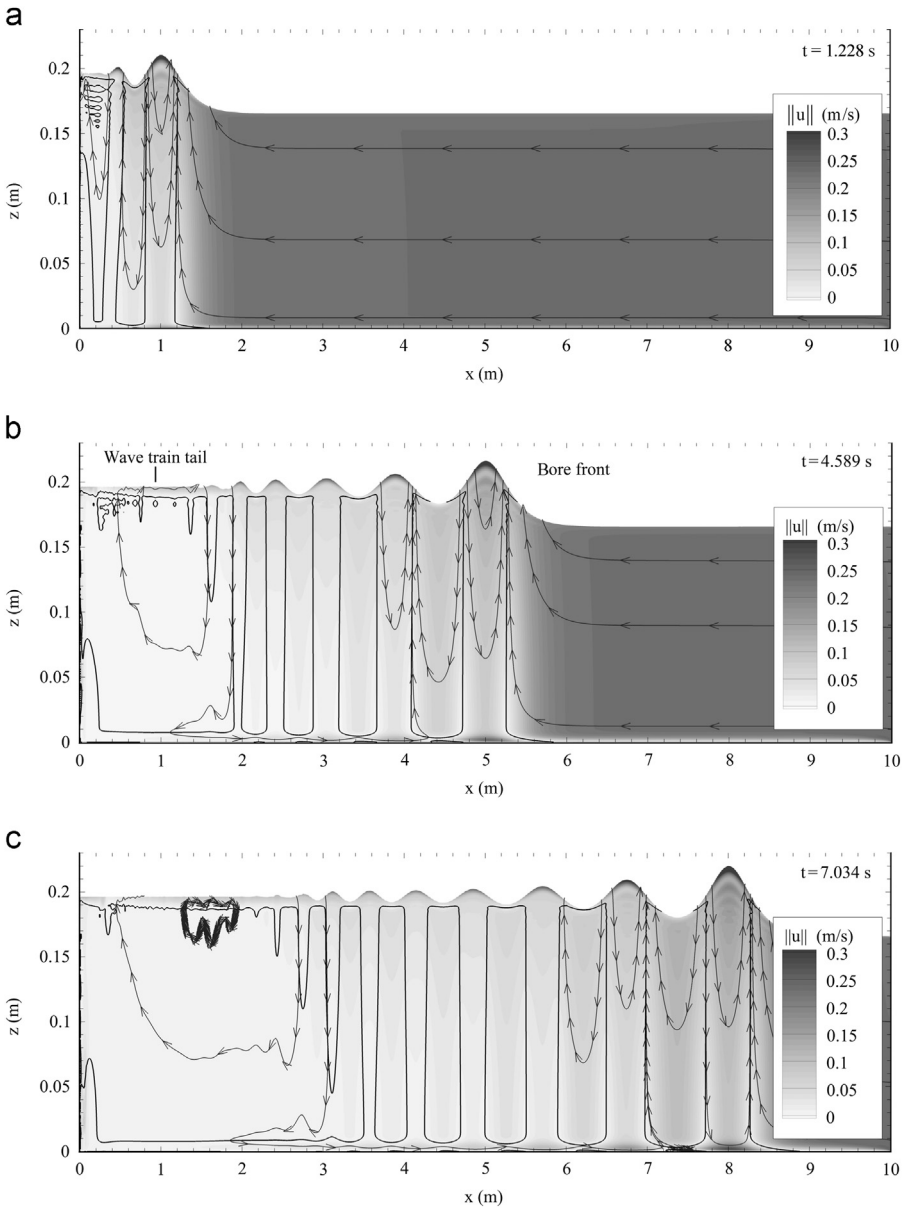


**Fig. 4.** Case A: dominated by undulations, mapping of the velocity magnitude ||u|| in the water during the bore propagation at 3 different times with velocity streamlines (lines with arrows) and the isoline $u_x = 0$ (black lines). Axis scales are independent.

became smooth and propagated upstream as an undular bore. As it propagated, more secondary undulations appeared. The tail of secondary undulations never detached from the gate during the propagation of the bore in the 10 *m* long domain, contrarily to the one observed in the simulation of Case A. Within 20 cm from the gate, the flow remained tumultuous with occasional splashing and air entrainment. The mean average water depth near the gate slightly increased by 2–3 cm as the bore propagated between 2 to 8 m from the gate. From one secondary undulation to another, both the wave amplitude and the wavelength decreased from the wave front to the wave tail (Fig. 5). The flow velocity evolved in synchronization with the free surface. The longitudinal component of the flow velocity, $u_x$, decelerated and re-accelerated beneath the wave crest and wave trough, respectively (Fig. 5) contrarily to Case A where $u_x$ changes direction. Beneath the bore crest, the flow was oriented downstream except close to the bed at $z < 2\,cm$ for Case B (Fig. 5). The recirculation reached a value up to $0.84 \times V_1$ ($u_x = 0.7$ m/s).

Downstream of the velocity reversal, spinning structures were ejected as the bore propagated (Fig. 6). The rotating structures appeared with a frequency of 10.5 Hz during the bore propagation and created local zones of low pressure (Fig. 6) as detailed in Simon (2013). The structures also had an effect on the vertical component of the flow velocity, $u_z$, that did not undulate in synchronization with the increase and decrease of the water depth but rather fluctuated quickly with the generation and ejection of eddies. In addition to the flow reversal near the bed, a strong flow deceleration took place 1 cm beneath the free surface crest with the horizontal component of the flow velocity, $u_x$, reaching -0.1 m/s. For this case, the flow mostly kept its initial direction beneath each crest and each trough except close to the bed beneath the crest where an intense flow reversal appeared. A more detailed analysis was presented in Simon (2013). Here, the flow was dominated by the initial current (Berchet, 2014).

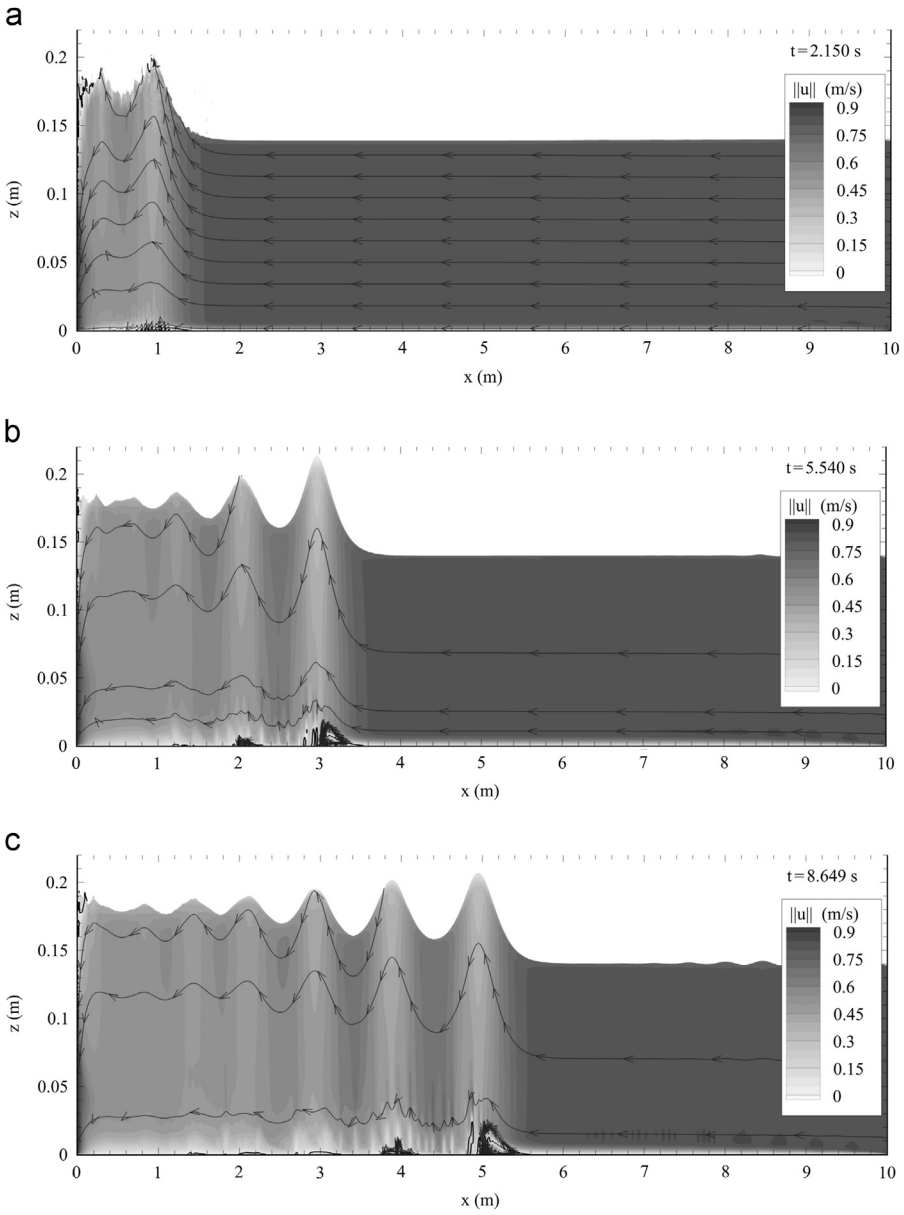


**Fig. 5.** Case B: dominated by the initial current, mapping of the velocity magnitude ||u|| in the water during the bore propagation at 3 different times with velocity streamlines (lines with arrows) and the isoline $u_x = 0$ (black lines). Axis scales are independent.

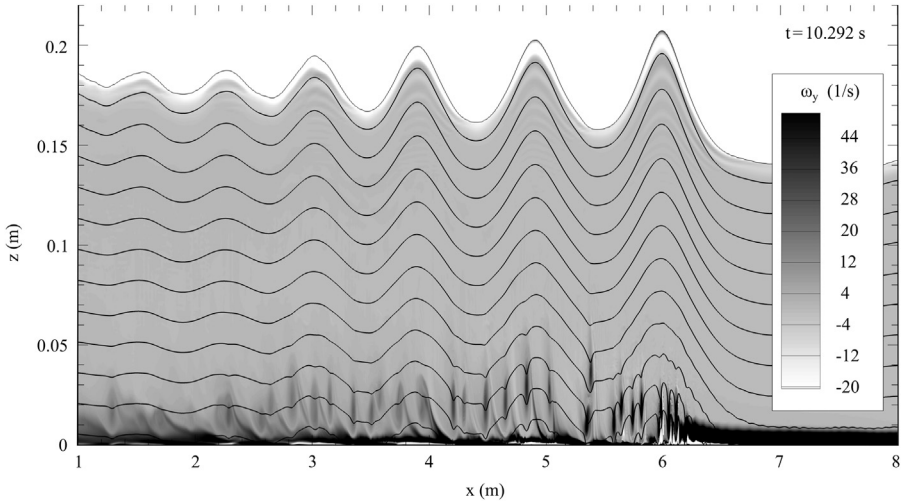


**Fig. 6.** Case B: vorticity field, $\omega_y$, beneath the bore with pressure isolines every 150 Pa (black lines).

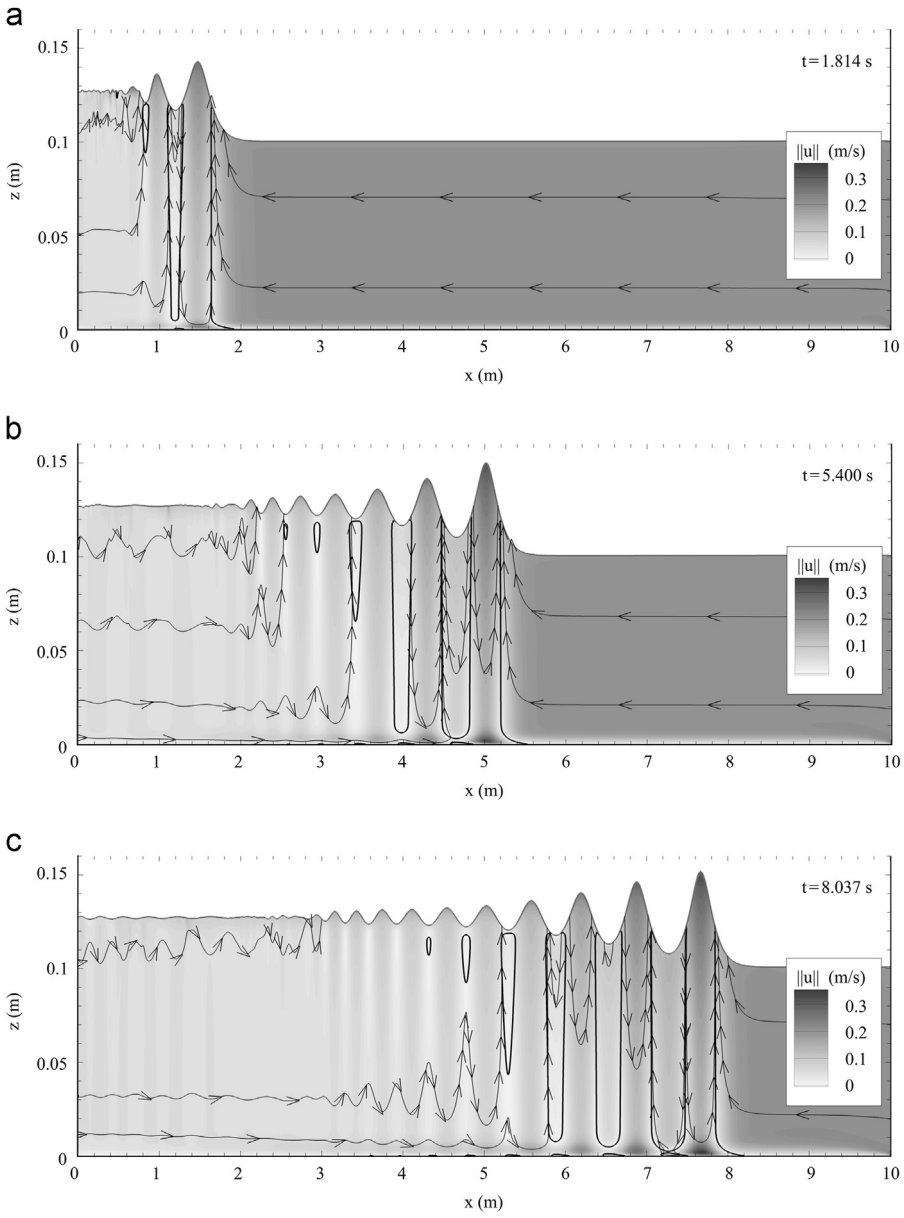


**Fig. 7.** Case C: partially dominated by undulations and then the bore flow, mapping of the velocity magnitude ||u|| in the water during the bore propagation at 3 different times with velocity streamlines (lines with arrows) and the isoline of $u_x = 0$ (black lines). Axis scales are independent.

### 3.3. Case C: hydrodynamics partially dominated by undulations and then bore flow

Case C started by the collapse of the higher water domain ($h_2 > h_1$ at $x = 0$) over the initial flow. The bore front quickly appeared and propagated upstream as an undular bore. The free surface evolution during the undular bore propagation is similar to Case A (already discussed) and Case D (to be discussed), with secondary undulations appearing progressively and detaching from $x = 0$ (Fig. 7). The conjugate height of the bore conjugate depth, $h_2$, also remained unchanged after the bore propagation. The flow evolution in Case C was a combination of Cases A and D.

Beneath the bore front and the first undulations, the flow was similar to Case A, with $u_x$ being positive beneath the crest and mostly negative beneath troughs (Fig. 7). As for Case A, under crests, $u_x$ was larger near the free surface and near the bed over the water column ($1.6 \times V_1$ and $1.5 \times V_1$, respectively, for the front at $x = 5\,m$). Beneath the secondary undulations, the surface of areas where $u_x$ was negative beneath the trough progressively diminished until the areas disappeared. For example, at the time $t = 8.037$ s, the longitudinal component of the flow velocity is positive under the seventh trough in Fig. 7 whereas the sixth trough shows an area with $u_x < 0$ (black isoline). In the following secondary undulations, the areas with $u_x < 0$ disappeared, the hydrodynamics of the flow were similar to those in Case D. The velocity was undulating in synchronization with the free surface with larger values beneath crests than beneath troughs and remaining positive.

Here, Case C was an intermediate case between a flow dominated by the undulations and dominated by the bore flow.

### 3.4. Case D: hydrodynamics dominated by the bore flow

Case D started with the collapse of the higher water domain ($h_2 > h_1$ at $x = 0$ m) over the initial flow. The bore front quickly appeared and propagated upstream as an undular bore. The water level evolution during the bore propagation was similar to Case A, with secondary undulations progressively appearing and detaching

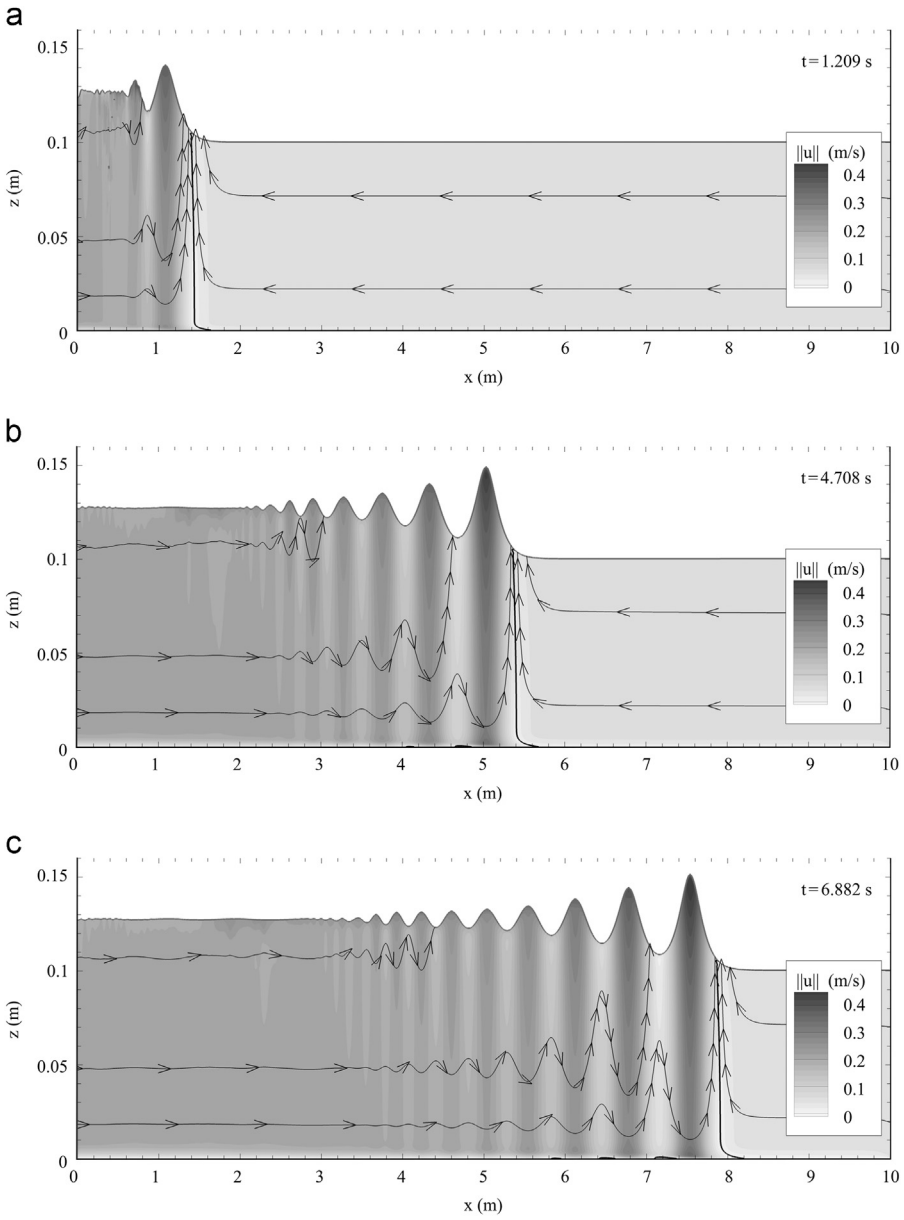


**Fig. 8.** Case D: dominated by bore flow, mapping of the velocity magnitude ‖u‖ in the water during bore propagation at 3 different times with velocity streamlines (lines with arrows) and the isoline of $u_x = 0$ (black lines). Axis scales are independent.

from $x = 0\,m$ (Fig. 8). The height of the bore conjugate depth, $h_2$, remained unchanged after the bore propagation. In this case, the flow evolution was simpler than for the two previous cases. Looking at Fig. 8, a complete flow reversal over the complete water column is seen during the bore passage. However, by looking closely at the flow hydrodynamics near the bed, a change of direction of the velocity appears near the bed ($z < 1$ mm) under the first troughs.

During the bore passage, the horizontal component of the flow velocity, $u_x$, was larger beneath the crest than beneath the trough (Fig. 8). Beneath crests, the velocity was more intense both near the free surface and near the bed than in the rest of the water column, with values reaching $8.8 \times V_1$ and $6.6 \times V_1$ near the surface and the bed, respectively, for the front crest at $x = 5$ m. For the following secondary undulations, the longitudinal component of the flow velocity followed a similar pattern to the one observed beneath the first wave crest and trough with a stabilization of the flow velocity around $V_2$. For this case, the flow suddenly changed direction beneath the bore front and undulated regularly after the bore front. Here, the flow was dominated by the bore flow.

### 3.5. Summary

Fig. 9 illustrates the flow hydrodynamics when the bore propagates as based on the results shown in Figs. 4, 5, 7 and 8. For Cases A and C, the direction of the longitudinal component of the flow velocity alternates under the crest and the trough. For Case B, no reversal of the longitudinal component of the flow velocity occurs in the water column, whereas for Cases D, a complete flow reversal occurs under the bore front with exception near the bed for Cases B and D. This reversal near the bed can generate loops of streamtraces as shown in Fig. 5. Table 3 lists a summary of the noticeable hydrodynamic flow properties.

Visual observations of tidal bores highlight the turbulent nature of the phenomenon. Some energetic turbulent events are observed in natural rivers due to the breaking bore front and to some forms of macro-turbulence likely induced by secondary motion. River morphologies are mostly irregular: meanders can be responsible for the generation of large macro-recirculation, which then propagate following the river stream, and the 3D bathymetry

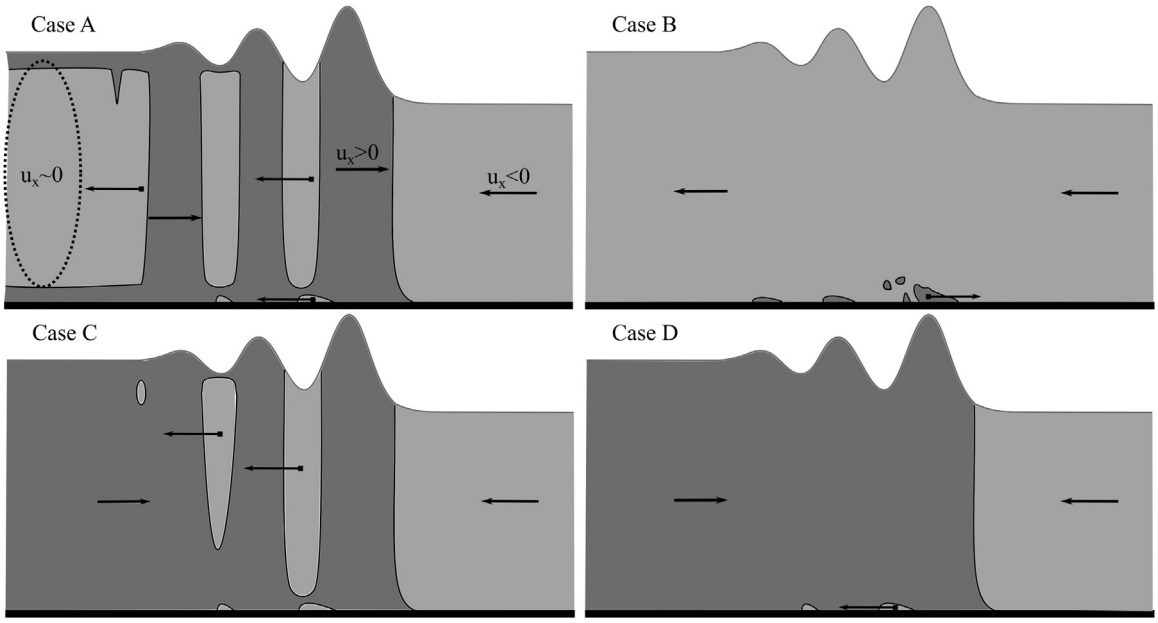


**Fig. 9.** Simplified schemes of the longitudinal component of the flow velocity when the bore is developed. Focus on the bore front and its first stubbles. The dark gray area represents a region with $u_x > 0$ and the light gray area represents $u_x < 0$. The black lines are for $u_x = 0$.

**Table 3**
Summary of the bore hydrodynamic properties as seen in Fig. 9. Based on computational results obtained at $x = 6.15$ m, $a_w$ is the wave amplitude calculated as half the vertical distance between the crest and the trough of the bore front.

| Case | $V_b$ (m/s) | $h_1/d_2$ | $a_w/h_1$ | Key properties |
|---|---|---|---|---|
| A | 1.22 | 1.206 | 0.115 | Inversion beneath crests and troughs, strong shear near the bed, incomplete inversion near the bed beneath the trough. Effects dominated by undulations. |
| B | 0.625 | 1.314 | 0.181 | Flow with mostly no change in direction, strong inversion ($u_x > 0$) near the bed beneath the crest, ejections of eddies. Effects dominated by the initial current. |
| C | 1.003 | 1.269 | 0.209 | Flow inversion with the bore passage, with flow reversal beneath the wave trough (same direction as $V_1$). Mix of A and D. Effects dominated by undulations then by the bore flow. |
| D | 1.152 | 1.269 | 0.204 | Complete change of the current direction, strong shear near the bed, small area of flow inversion ($u_x < 0$) near the bed beneath first troughs. Effects dominated by the bore flow. |

generates hydrodynamic structures at the bed, which can be related to kolk-boils or bursting events ejected upwards from the 3D river bed macro-irregularities. Many authors accounted for the violence of the tidal bore flows, where repeated field work accidents were reported in the literature with lost or damaged units and buried equipment (Chanson & Lubin, 2013).

Some very unusual features have also been reported, like tidal bore collisions (Bonneton et al., 2011; Destriau & Destriau, 1951; Keevil et al., 2015; Reungoat et al., 2014) or delayed flow reversals (Bazin, 1865a, 1865b; Partiot, 1858, 1861; Reungoat et al., 2012). Reungoat et al. (2012, 2014) quantified and analyzed the flow reversal delay between the bore front passage and longitudinal flow reversal. The measurements showed the reversal in longitudinal flow direction to be about 50 s after the bore front, while the free-surface velocity next to the survey staff reversed direction about 6 s after the bore front. These recent studies confirm past observations in the Seine River (France), where some field observations were undertaken in the 1850s by Partiot (1861): Floats were introduced at several heights prior to the arrival of the tidal bore. The float direction was observed after the bore passage. In one case, the surface float continued to float downstream for about 120 s after the bore, while the bottom float flowed downstream only for 90 s. Afterwards the floats flowed upstream.

In the Severn River (UK), some delayed flow reversal was also reported depending upon the relative water elevation and bore strength (Robowtham, 1964):

The water near the bed still flowing downwards for up to ten minutes after the surface has been suddenly reversed by the passage of a fairly large bore, with small bores the normal downward flow comes gently to a standstill after the bore had gone by and it may be a minute before the upward stream gathers momentum.

An unusual flow reversal pattern also was reported in the Rio Mearim (Brazil) by Kjerfve and Ferreira (1993): At times, the downstream flow resumed after passage of the bore for another 30 s before the flow again surged upstream. This observation was based upon measurements at 0.7 m above the bottom, whereas an early flow reversal was further reported: the current began changing directions 60 s ahead of arrival of the bore.

The foregoing observations confirm that very complicated and local features can be associated with tidal bore propagation. Thus, each tidal bore is almost unique and relevant to the place where it has been observed, even if some trends are common. The classification proposed in Table 3 can be related to the physical tidal bore observed in physical modelling (laboratory experiments) or in situ observations. Cases A and B can be related to laboratory experiments, where no flow reversal is usually observed. Most of the laboratory experiments with closing gate are related to Case B where the river current is dominant on the hydrodynamics. Cases C and D allow for flow reversal, as experienced in nature (Furgerot et al., 2016). Fig. 5 presented by Rousseaux et al. (2016) highlights the flow dominated by undulations, where hydrodynamic structures can be seen below the stubbles' troughs (Case C).

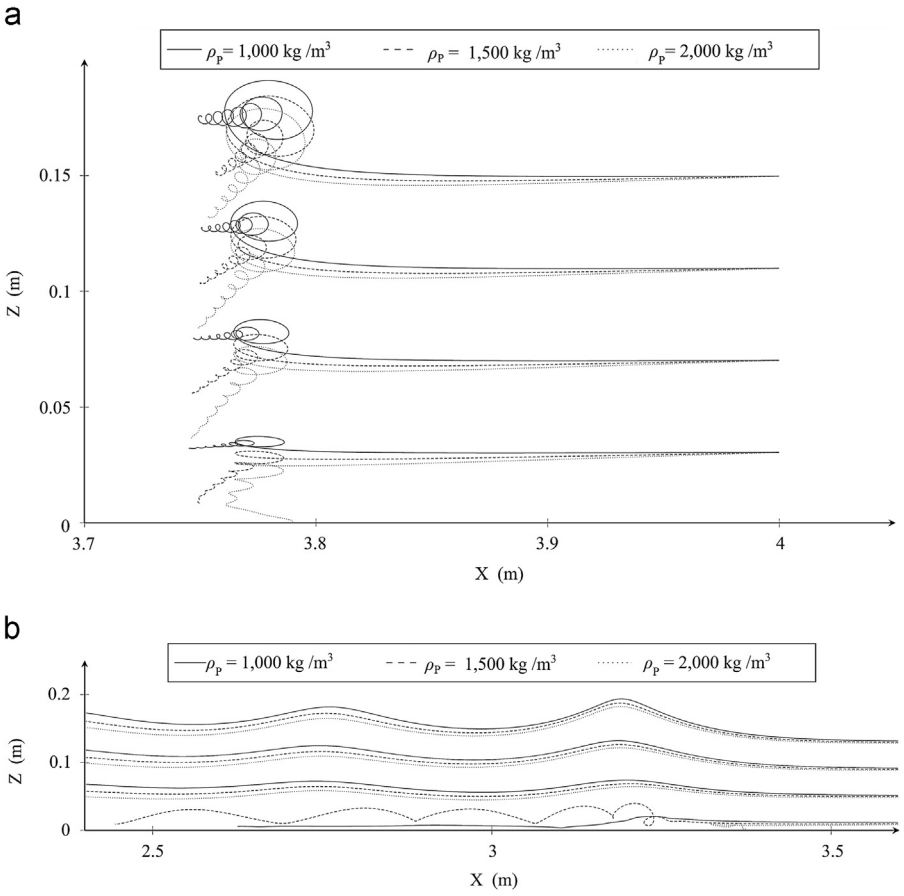


**Fig. 10.** Trajectories of suspended particles during the passage of the bore at different injection heights and different densities (Top: Case A and bottom: Case B).

## 4. Particle trajectories

### 4.1. Presentation of the case studies

In this section, the characteristic trajectories of suspended particles during the passage of the bore are studied. First, the dispersion of suspended particles due to the sub-grid turbulence briefly is assessed and then the trajectories of particles injected at different heights and with different densities will be characterized.

In order to model the effect of small scale turbulence on the particles, a random velocity component usually is added to the deterministic velocity computed from the Maxey and Riley (1983) equation. The norm of this random component depends mainly on the mass of suspended particles and on the turbulent viscosity (Pozorski & Minier, 1998; Wang & Squires, 1996). A test was conducted by injecting 10,000 suspended particles at ($x = 4$ m, $z = 5$ m) in order to quantify the effect of this random component on the global trajectories of particles. The simulated trajectories, affected or not by turbulent dispersion, are extremely close. This is the result of very low values of turbulent dispersion in the area where the suspended particles move. High values of turbulent dispersion are only observed near the free surface of the bore and very close to the river bed (for $z \leq 2$ mm). In the worst case, the standard deviation of the suspended particle positions after 4 *s* of simulation is equal to 0.2 mm (obtained from the 10,000 suspended trajectories). This deviation is negligible compared to the global movement. Therefore, the turbulent dispersion is neglected in the following analysis. The study of trajectories of suspended particles is, thus, done by removing the random part of motion due to the sub-grid turbulence, thus the analysis represents the average trajectories of each particle type, and the trajectories obey to the standard Maxey and Riley (1983) equation.

Also, it is assumed that the number of suspended particles per unit volume is small, so the fluid disturbance due to the particles is neglected in this study. In all Cases (A, B, C, and D), the particles are injected at $x = 4$ m at heights $z = 1$, 3, 5, 7, 9, 11, and 13 cm. The choice of the abscissa $x$ does not influence the form of particle trajectories. The densities of these particles range from 1000 to 2,500 kg/m$^3$. Typically, fluid particles and granular materials like sand can be modeled. As the Stokes number is around $10^{-3}$ (based on a typical length of stubbles, secondary waves on the order of half a meter), the particles behave as buoyant tracers. Fig. 10 (Top: Case A and bottom: Case B) shows the trajectories of these particles in Cases A and B for different densities.

### 4.2. Maxey and Riley (1983) equation

In this study, the interactions particle/fluid and particle/particle are assumed to be negligible. Thus, the trajectory of each particle can be described by the fundamental principle dynamics as follows:

$$\frac{d\mathbf{x}_i}{dt} = \mathbf{v}_i(t), \tag{8}$$

$$m_i \frac{d\mathbf{v}_i}{dt} = \sum_j \mathbf{F}_j \tag{9}$$

where $m_i$, $\mathbf{x}_i$, and $\mathbf{v}_i$ are the mass, the position, and the velocity of each particle, respectively. In order to be close to reality, various forces, $\mathbf{F}_j$, applied to the particle are considered here. The force $\mathbf{F}_{GB}$ of gravity and buoyancy are introduced by:

$$\mathbf{F}_{GB} = V_i\left(\rho_p - \rho_w\right)g\mathbf{z} \tag{10}$$

where $\rho_p$ is the density of particles, $V_i$ is the volume of each particle, and $\mathbf{z}$ is the vertical unit vector of the axis system.

The added mass, $\mathbf{F}_{MA}$, reflects that the motion of one particle induces the motion of the fluid surrounding it (Bessel, 1826; Poisson, 1831). The added mass is described by:

$$F_{MA} = \frac{m_w}{2}\left(\frac{dv_i^*}{dt} - \frac{Du_i}{Dt}\right) \text{with } v_i^* = v_i - u_i \tag{11}$$

where $\mathbf{u}_i$ and $m_w$ are the flow velocity of water at the location of each particle and the mass of water contained in the volume of each particle, respectively. In this expression, the last term of the second member was proposed by Auton et al. (1988) to take into account the effect of the velocity gradient around particles. Minier (1988) showed that this expression is valid for a particle size smaller than the Komolgorov scale (Davidson, 2015; Kolmogorov, 1961).

The viscous drag, $\mathbf{F}_T$, reflects the effect of the viscosity on the particles (Stokes, 1845), which makes the particle be entrained by the fluid. If the density of the particle is the same as the fluid, the drag makes the particle follow the streamlines. Otherwise, the trajectory of the particle separates from the streamlines because of inertia. The viscosity drag is given by Michaelides (1997) as follows:

$$F_T = -\frac{1}{2}C_D\pi\rho_w r_i^2\|v_i^*\|v_i^* \text{ with } C_D = \frac{24(1+0.15Re_p^{0.687})}{Re_p} + \frac{0.42}{1+4.2510^4 Re_p^{-1.16}} \tag{12}$$

where $Re_p$ and $r_i$ are the particle Reynolds number and the radius of each particle, respectively, and $C_D$ is the viscous drag coefficient. The expression for $C_D$ given by Clift et al. (1978) is valid for $Re_p < 3.10^5$.

The Basset (1888) history force, $\mathbf{F}_H$, reflects the effect of the settling time of the boundary layer around the particle on its dynamics, and is given by:

$$F_H = -6\pi r_i^2\mu_w\int_0^t\frac{d}{dt}\left(v_i^* - \frac{1}{6}r_i^2\nabla^2 u_i\right)\frac{d\tau}{\sqrt{\pi\nu_w(t-\tau)}} \tag{13}$$

where $\nu_w$ is the dynamic viscosity of water. The influence of this force can become very important when the density of particles, $\rho_p$, is close to the density of water, $\rho_w$. The term $\nabla^2\mathbf{u}_i$ is a corrective term introduced by Faxen (1922) to take into account the non-uniformity of the velocity field around a particle. As the particle size is smaller than the Komolgorov scale, this term is negligible.

Finally, the system of equations governing the trajectory of one particle is given by:

$$\frac{dx_i}{dt} = v_i(t), \tag{14}$$

$$\frac{dv_i}{dt} = -\frac{1}{2\rho_p+\rho_w}\left(\frac{9\rho_w}{r_i}\sqrt{\frac{\nu_w}{\pi}}\int_0^t\frac{dv_i^*}{d\tau}\frac{d\tau}{\sqrt{t-\tau}} - \left(2\left(\rho_p-\rho_w\right)g - 3\rho_w\frac{Du_i}{Dt} + \frac{3\rho_w}{4r_i}v_i^*\|v_i^*\|C_D\right).\right) \tag{15}$$

where $\tau$ is the integration variable taken in the range $[0, t]$. In the literature, the second equation is called the modified Maxey and Riley (1983) equation. The initial form of this equation was given by Maxey and Riley (1983). The system of equations is solved using a fourth-order Runge-Kutta scheme. A parameter study, not presented here, has allowed the time step $\delta t$ to be fixed. A good compromise between the CPU time and accuracy is $\delta t = 0.01$ s. As the code Thetis provides access to a discrete velocity field at a given time, temporal and spatial interpolations are used to evaluate the velocity at the location of the particles at any time. A linear function and a B-spline function are used for the temporal and spatial interpolations, respectively (Deutsch, 1992).

### 4.3. Numerical results

#### 4.3.1. Case A: trajectories dominated by undulations

In the upper part of the flow (Fig. 10 - Top), above the boundary layer and the inversion region of the current, because of the sudden stop of the flow after the front, the particle trajectories form spirals whose center is in a translation partly due to the current and partly due to gravity. In this case, all the particle trajectories whose injection height is greater than or equal to $z = 5$ cm have the same shape and differ only by the magnitude of the spirals. Such paths are called ribbon-like trajectories. However, the particles injected at $z = 1$ and 3 cm interact with the boundary layer and the current inversion zone described above and the spirals are either strongly deformed or disappear completely.

It is further noted that even in the case of particles of density equal to the fluid density (1000 kg/m$^3$), a downward motion appears after the passage of the front, which is not the case in the upper region. It is, therefore, a downward movement which is not due to gravity. In this flow, in particular, the turning area where the fluid velocity is directed from downstream to upstream is always present between 0 and 0.5 cm from the bottom after the passage of the front, although the velocity magnitude is weak ($\approx$ 0.035 m/s). This thin reversal layer induces a motion of suction on the particles between 0.5 and 2 cm above the bed, hence, the downward grain movement in this area.

#### 4.3.2. Case B: trajectories dominated by the initial current

On the contrary in Case B (Fig. 10 - Bottom), the mean flow velocity remains downstream and the particle trajectories do undulate while continuing downstream in the upper area. In this case, all the trajectories of particles have the same shape when the injection height is greater than or equal to $z = 3$ cm. Such paths are called undulating ribbon-like trajectories.

For the particles injected at $z = 1$ cm, the trajectories are much more complex due to the strong interactions with recirculation zones. One observes that the particles whose density is between 1500 and 2200 kg/m$^3$ may have quasi-ballistic trajectories that go up to a height of 3 to 4 cm. These trajectories are very similar to those of saltating particles and are the result of the vertical drive of particles by successive recirculation zones which induce high vertical acceleration. When this recirculation zone moves simultaneously with the tidal jump, the particles maintain a significant vertical component due to their inertia, which induces the quasi-ballistic trajectories observed. The light particles, whose density is less than 1500 kg/m$^3$, do not have sufficient inertia and follow the flow again as soon as they go outside of the recirculation zone. On the contrary, heavy particles whose density is greater than 2200 kg/m$^3$ are not sufficiently accelerated and continue their sedimentation even in these areas.

#### 4.3.3. Case C: trajectories partially dominated by the bore flow and then the initial current, and Case D: Trajectories dominated by the bore flow

Compared to the two previous cases, the two cases denoted C and D present a different behavior for the trajectories of suspended particles. When the bore front passes, the direction of particle trajectories is inverted. This inversion of the direction of paths was observed for all densities tested, $1000 < \rho_p < 2500$ kg/m$^3$, and all injection heights tested, $1 < z < 13$ cm (Figs. 11 and 12). The inversion is due to the flow reversal observed over the complete water column during the bore passage in both Cases C and D (Figs. 7 and 8).

In Case C, during a short duration after the bore front passage, the trajectories of suspended particles form undulations similar to elongated trochoids oriented downwards (Fig. 11). A few moments after the bore passage, the form of these trajectories looks like the

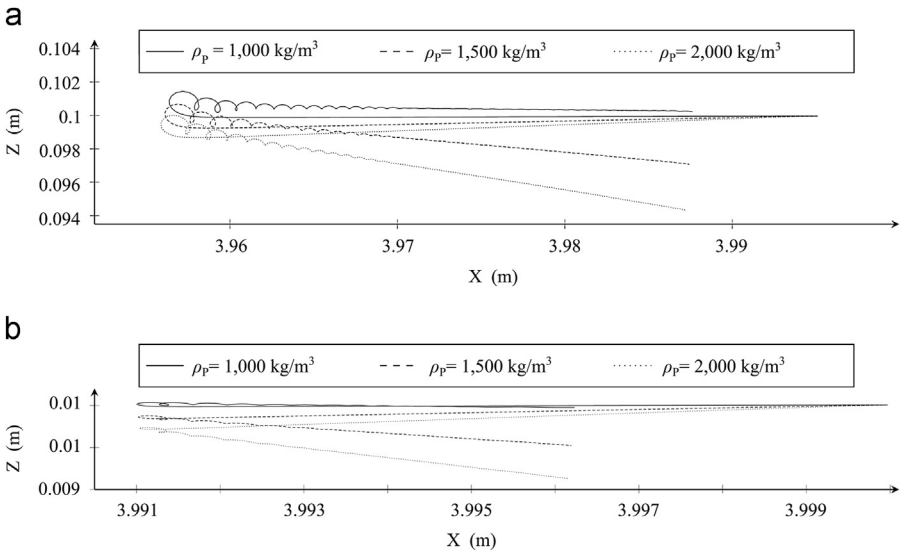


**Fig. 11.** Case C, trajectories of suspended particles at $z = 0.01$ cm (bottom) and 0.1 cm (top) during the bore passage for different densities.

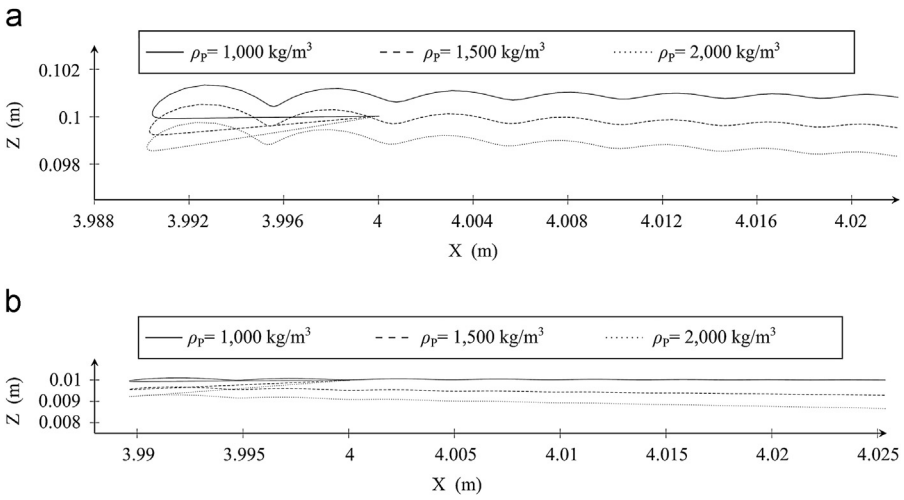


**Fig. 12.** Case D, trajectories of suspended particles at $z = 0.01$ cm (bottom) and 0.1 cm (top) during the bore passage for different densities.

one for Case D. Case C is a combination of Cases A and D. The flow is partially dominated by the bore flow (Fig. 7). As in Case D, the magnitude of undulations is reduced with the time and the injection height of suspended particles.

In Case D, after the bore passage, the trajectories form undulations similar to cycloids oriented downwards (Fig. 12 - top). Reducing the injection height of suspended particles yields a reduction of the magnitude of undulations (Fig. 12 - bottom). This observation highlights an attenuation of the influence of the bore flow on the water column induced by the boundary layer located at the bed of the channel. The magnitude of undulations also reduces with the time (Fig. 12). The secondary undulations of the free surface have a magnitude lower than that for the undular bore (Fig. 8).

## 5. Modified Chen's model

### 5.1. Description of the model

The forms of particle trajectories observed in the upper part ($z \geq 5$ cm) are very similar to those encountered in the framework of the wave-current interactions problem (Chen et al., 1964, 2010, 2012; Chen & Chen, 2014; Hsu, 2016). In these studies, the current is assumed to be constant, the wave is established and these studies limit themselves to the monitoring of water particles, which, in the current study, is equivalent to particles of a density $\rho_p = \rho_w = 1000$ kg/m$^3$. The equations for the water particle trajectories resulting from the current study are complex and are given in the Appendix. To characterize these trajectories, $U$ is the speed of a uniform steady flow, $V$ is the wave propagation velocity, and $V_p$ is the maximum speed of a particle induced by the same wave propagating in the fluid at rest. From these designations, five main regimes can be distinguished when:

- the wave propagates in the same direction as the flow and $\|V\| > \|U\|$, the trajectories form elongated trochoids oriented downwards (Fig. 13a). A trochoid is a curve of equations $x(t) = a\,t - b\sin(t)$ and $z(t) = a - b\cos(t)$. It is called extended when $a < b$ and shortened when $a > b$.
- the wave propagates in the same direction as the flow and $\|V\| = \|U\|$, the trajectories form cycloids oriented downwards (Fig. 13b).
- the wave propagates in the direction opposite to the flow and $\|V\| > \|U\|$, the trajectories form elongated trochoids oriented upwards (Fig. 13c).

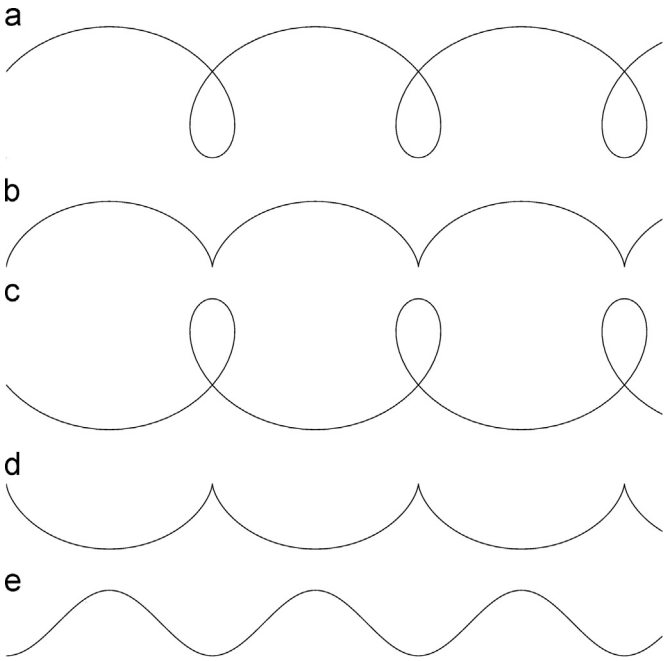


**Fig. 13.** Different types of fluid particles trajectories for several flows in presence of the wave-current interaction (after Chen et al., 1964, 2010, 2012; Chen & Chen, 2014; Hsu, 2016).

- the wave propagates in the direction opposite to the flow and $\|V\| = \|U\|$, the trajectories form cycloids oriented upwards (Fig. 13d).
- when the wave propagates at a much lower speed than the flow, regardless of its direction, the wave effect is small and $\|V\| < \|U\|$. The trajectories then form undulations (Fig. 13e).

### 5.2. Application of the model

The theories developed in this context are, therefore, unable to reproduce all the features of trajectories encountered in a bore. However, simple changes, applied to these theories, should allow to improve the conceptual modeling of simulated particles trajectories. The characteristics of simulated particle trajectories are the following:

- a horizontal trajectory at a speed $V_p$ without undulations before the jump passage.
- an over-elevation of the mean height during the jump passage going from $h_1$ to $h_2$.
- a velocity slow-down during the jump passage going from $V_1$ to $V_2$.
- oscillations around the mean height during the passage of every stubble with a progressive attenuation.
- a vertical downward drift due to gravity.

These different elements are shown schematically in Fig. 14. Note that in both cases, all the elements are the same except the part on the wave-current interaction.

The equations proposed by Chen et al. (1964, 2012) can describe the wave-current interaction for both cases: only one equation is needed to describe the particle trajectories in the upper part of the undulating bore, regardless of the mode generation. All of these elements can be described individually by corresponding equations. The transition taking place at the front is represented by a hyperbolic tangent, which allows the computations to go from state 1, before the jump, to state 2 after the jump in a continuous manner. Here, it is proposed to separate the different contributions in order to quantify each of them, in Cases A and B. The model presented is not intended to accurately reproduce the trajectories of suspended particles but will help in understanding the different contributions to this phenomenon. The parameter values which are used during this decomposition are listed in Table 4.

The first characteristic which is simple to isolate is the contribution due to gravity. Considering that the sedimentation velocity is constant, this contribution is of the form $z(t) = -w_s(t-t_0)$ where $t_0$ is the initial time of the trajectory and $w_s = 0.007$ m/s the sedimentation velocity for a particle density, $\rho_p = 2500\,\mathrm{kg/m^3}$ with a drag coefficient obeying the formula developed by Clift et al. (1978). By subtracting this contribution to the complete trajectory, a new path is obtained that is not affected by gravity, even for a particle whose density is different from the density of the fluid (Fig. 15).

The second characteristic is the elevation as well as the current slowing down at the bore passage. They can be considered in the same equation in which the height changes from $h_1$ to $h_2$ and the current velocity changes from $V_1$ to $V_2$. The particles studied being small, their velocities remain very close to that of the flow, including the horizontal component, the current slowing down translates directly into a particle slowing down. The contribution due to elevation will have a hyperbolic tangent shape and the one due to slowing down will be described by the integral of a hyperbolic tangent:

$$x(t) = \beta_1(V_1+V_2)t + \frac{1}{2\beta_1}((V_1-V_2)\log\left(\cosh(-\beta_1 t_B)\right) - \log\left(\cosh(\beta_1(t-t_B))\right)),$$
$$z(t) = \frac{h_2-h_1}{2}\tanh(\beta_2(t-t_B)) \qquad (16)$$

where $t_B$ is the time when the particle goes through the jump front, $\beta_1$ is the parameter controlling the speed of the slowdown between the two states before and after the front, and $\beta_2$ is the parameter controlling the speed of the change in elevation between the two states. Fig. 16 shows the new trajectory when this contribution is subtracted and compared to the previous one for which the gravity has already been removed. This new trajectory is very similar to the trajectories observed by Scott Russell (1845) in the case where he called the negative solitary wave of first order (Figs. 7–10 of Scott Russell (1845)).

Finally, the oscillations represented by a trajectory featuring the wave-current interaction and the gradual attenuation can be put in the form:

$$x(t) = x_{Chen}(t)\exp(-\beta_3(t)) \text{ and } z(t) = z_{Chen}(t)\exp(-\beta_3(t)) \qquad (17)$$

where $\beta_3$ is the attenuation parameter and ($x_{Chen}$, $z_{Chen}$) are the solutions proposed by Chen et al. (1964, 2012) and given in the Appendix. The parameters used in these equations are those of the flow after passage of the jump front. The trajectory determined from these equations is compared with the one of the particle after the passage of the jump front in Fig. 17. This simple model can reproduce the shape of particle trajectories as they pass under the stubbles but is less valid near the front. This poorer agreement near the front is explained by the peculiar hydrodynamic effects associated with the front propagation that are not represented in this model and also because the model is supposed to represent the trajectories of water particles and not of suspended particles whose density is different from that of water. These equations are a good approximation of the trajectory after the passage of the jump when the contribution of gravity has been withdrawn. However, they cannot give precise solutions since the inertia of

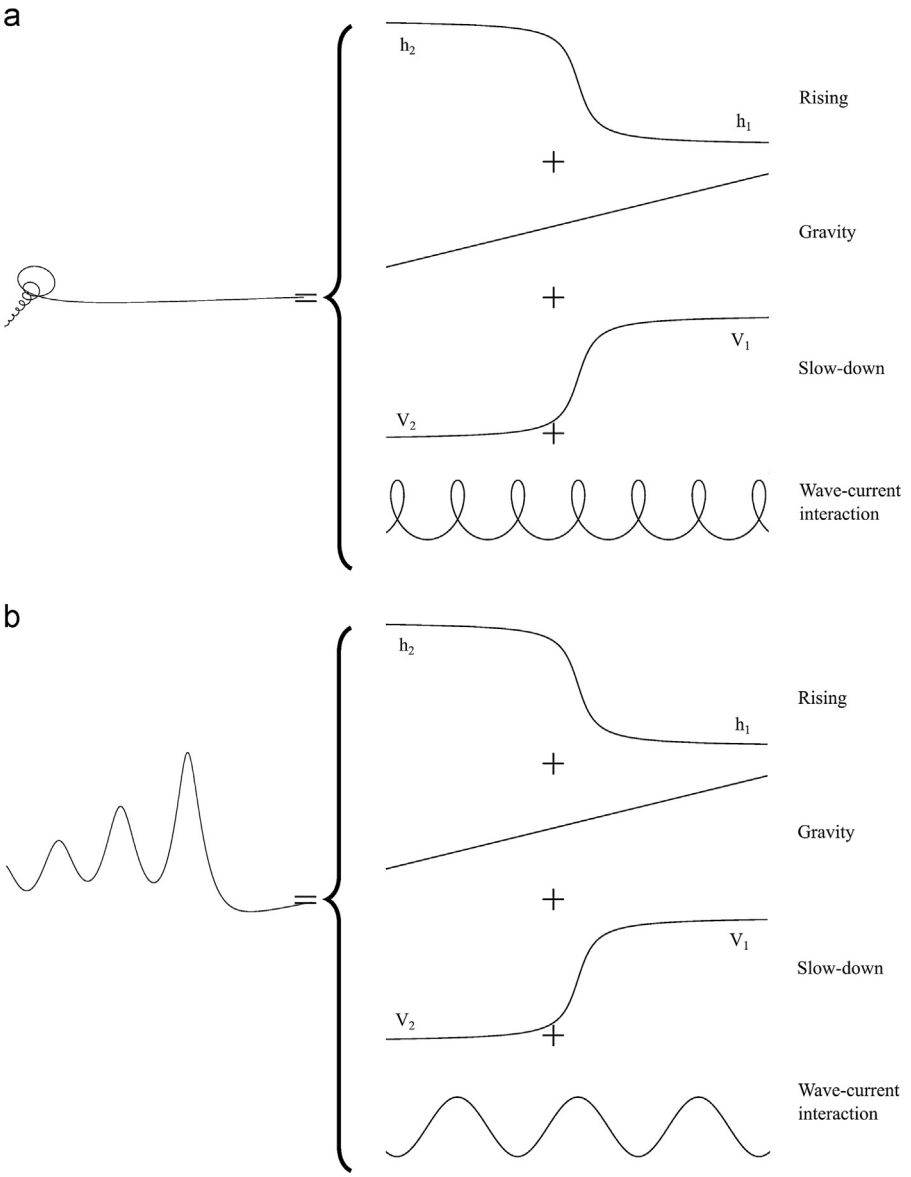


**Fig. 14.** The features of trajectories encountered in the two cases studied without reversal (Top: Case A and bottom: Case B).

**Table 4**
Parameters used for the decomposition of particle trajectories.

| Parameter | Definition | Case A | Case B |
|---|---|---|---|
| $t_B$ | Time when the particle goes through the jump front | 3 s | 5.5 s |
| $w_s$ | Sedimentation velocity of suspended particles | $7.1e^{-3}$ m/s | $7.1e^{-3}$ m/s |
| $\beta_1$ | Parameter controlling the speed of the slowdown between the two states before and after the front | 1.1 | 1.5 |
| $\beta_2$ | Parameter controlling the speed of the change in elevation between the two states before and after the front | 9.37 | 4.87 |
| $\beta_3$ | Attenuation parameter | 0.605 | 0.63 |

particles and several terms of hydrodynamic forces, such as the drag, the added mass, and the Basset history force were implicitly neglected. Nevertheless, this decomposition allows the different contributions to be distinguished.

The same operations applied to Case B also help to decompose the suspended particles trajectory. The steps are shown in Figs. 18–20 whose parameters are listed in Table 4. In this case too, the proposed model allows the different components to be separated satisfactorily. Further studies would be required, however, because here the number of stubbles passed through by the particles is too small (only 3) in order to draw a generalized conclusion.

## 6. Conclusions

The tracking of individual trajectories of suspended particles enabled simulation of the trajectories of these particles for different densities and to propose a model to decompose these

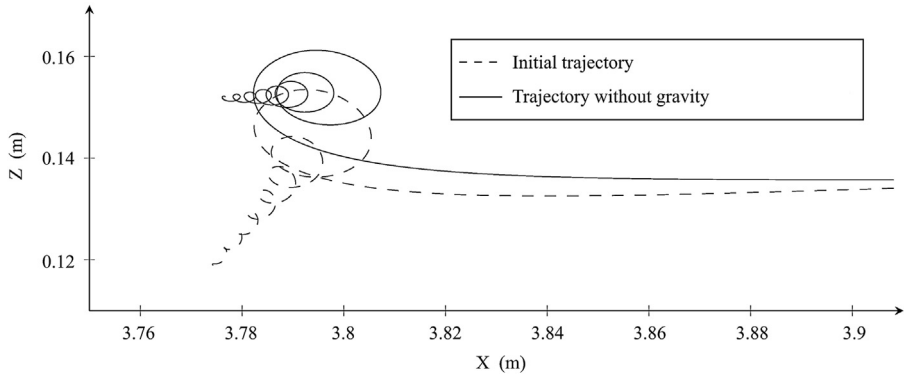


**Fig. 15.** Comparison of the full trajectory to the one whose contribution due to gravity was removed (Case A).

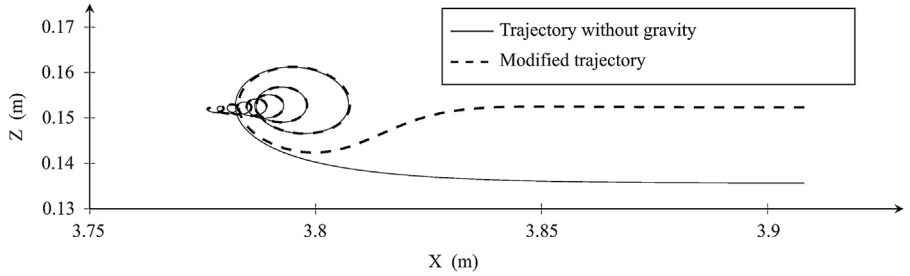


**Fig. 16.** Comparison of the trajectory without the contribution of gravity to the trajectory where the contributions of gravity, elevation, and the slowing down have been removed (Case A).

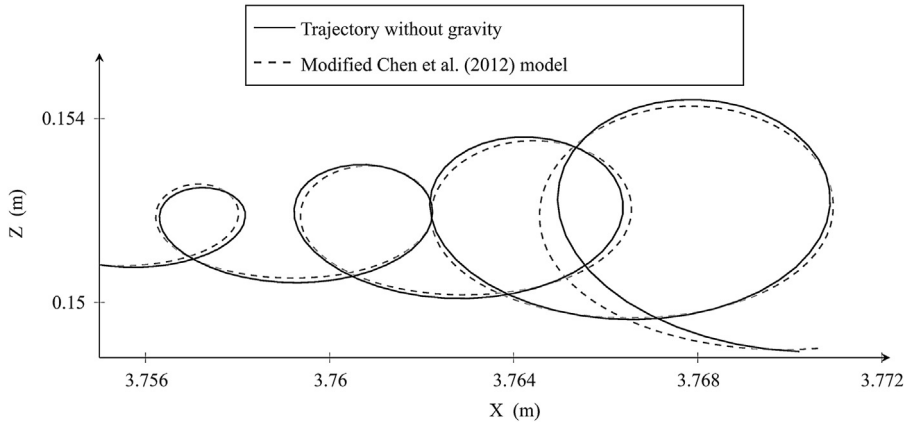


**Fig. 17.** Comparison of the trajectory without the contribution of gravity in the area following the passage of the bore front to the trajectory deduced from the wave-current interaction model including attenuation (Case A).

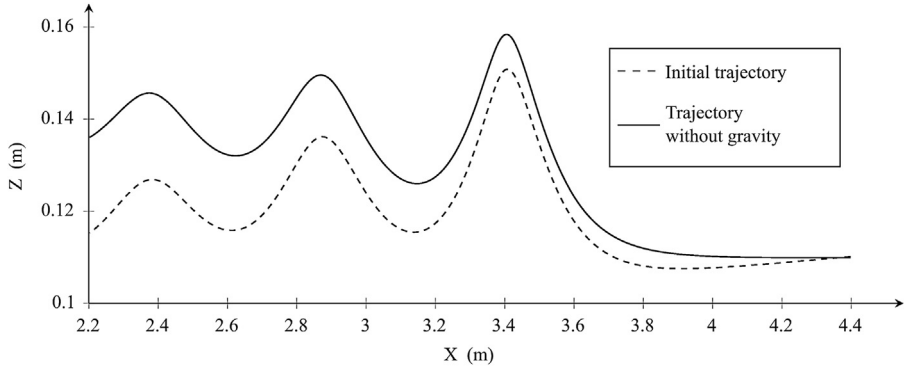


**Fig. 18.** Comparison of the full particle trajectory to the one with the contribution of gravity removed (Case B).

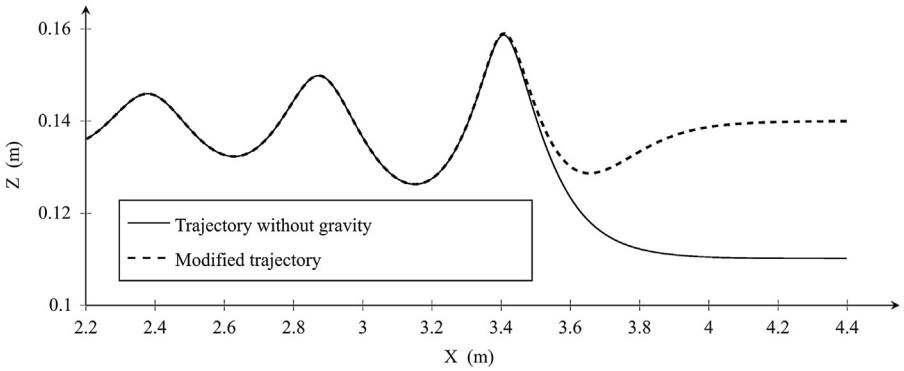


**Fig. 19.** Comparison of the trajectory without the contribution of gravity to the trajectory where the contributions of gravity, elevation, and the slowing down have been removed (Case B).

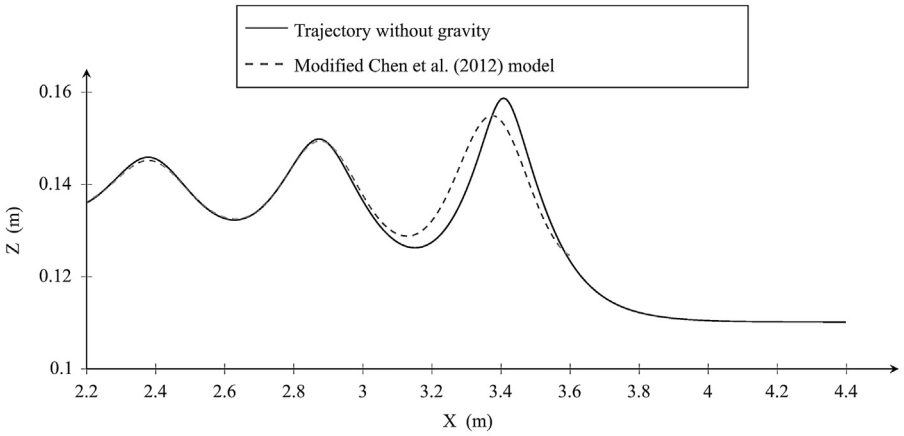


**Fig. 20.** Comparison of the trajectory without the contribution of gravity in the area following the passage of the bore front to the trajectory deduced from the wave-current interaction model including attenuation (Case B).

**Table 5**
Proposed classification of trajectories.

| | Without global reversal (counter-flowing) | With global reversal (co-flowing) |
|---|---|---|
| Flood dominated | Case A: upwards enrolled ribbon-like trajectories, Chen's model: (c) + (d) | Case C: downwards enrolled ribbon-like trajectories, Chen's model: (a) + (b) |
| Stream dominated | Case B: undulating ribbon-like trajectories, Chen's model: (e) + (d) | Case D: undulating ribbon-like trajectories, Chen's model: (e) + (b) |

observed trajectories as long as they do not fall within the area of the influence of the boundary layer. This model allows the importance of certain aspects of tidal bores to be highlighted. Four types of trajectories were observed (see Table 5). Without reversal, the trajectories are upwards enrolled ribbon-like in the case dominated by the flood (Case A) and ribbon-like undulating in the case dominated by the stream (Case B). With reversal, the trajectories are downwards enrolled ribbon-like in the case dominated by the flood (Case C) and ribbon-like undulating in the case dominated by the stream (Case D). In the tested surges, supposedly close to an undular tidal bore, the effect of gravity seems constant. Furthermore, the inertial and Basset history effects are almost negligible in the long term, i.e. for a time $t \geq 0.5$ s, even though they have a major impact on the short-term sedimentation. Moreover, the proposed model suggests that the effect of the transition that occurs at the front on the trajectory of a suspended particle is highly localized and its path can ultimately be divided into three parts:

- before the jump front, the particle is advected horizontally by the constant flow and slowly settles because of its density that is higher than the density of the fluid.

- at the front jump, the jump transition from the speed $V_1$ to the speed $V_2$ and from the height $h_1$ to the height $h_2$ induces an uprising and a slowing of the particles.
- after the jump front, the particle trajectory takes a form known as part of the underlying wave-current interactions problem (Chen et al., 1964, 2012) which differs from a usual case only by the gradual attenuation of the secondary waves.

This intuitive decomposition, although probably invalid from a hydrodynamic point of view due to the very pronounced non-linearity of the phenomenon gives a good description of trajectories of suspended particles. It also suggests a modelling track of an undular tidal bore as the superposition of a current that slows down at the jump front, a heightening of the average level, and a

negative solitary wave described by Scott Russell (1845). This type of the flow was also studied by Bazin (1865a, 1865b), and Bazin and Darcy (1865), but Scott Russell (1845) gave a more detailed description and was also interested in the trajectories of tracers subject to this flow. As a perspective, the authors are currently studying the dependence of three $\beta_i$ coefficients in Chen's model with the Froude number, *Fr*.

## Acknowledgements

This work was granted access to the HPC (High Performan Computing) resources of CINES (Centre Informatique National de l'Enseignement Supérieur), under the allocation x20152a6104 made by GENCI (Grand Equipement National de Calcul Intensif). Computer time for this study was also provided by the computing facilities at MCIA (Mésocentre de Calcul Intensif Aquitain) of the Université de Bordeaux and of the Université de Pau et des Pays de l'Adour. The authors also acknowledge the financial assistance of the Agence Nationale de la Recherche (Projet MASCARET 10-BLAN-0911-01).

## Appendix A. Trajectory modeling of fluid particles within a wave-current interaction approach

Chen et al. (1964, 2012) proposed an analytical solution for the estimation of Lagrangian trajectories of fluid particles in the context of the wave-current interaction. For this, they considered a monochromatic wave propagating on a uniform steady flow over a horizontal impermeable bottom. The movement of the fluid is considered 2D and irrotational, and the wave propagates from the left to the right (Fig. A1). The authors suggest the problem in terms of Lagrangian variables *a* and *b* that define the original position of the fluid particle. For every time, *t*, the position $b = 0$ corresponds to the free surface and $b = -d$ is the channel bottom with *d* the rest fluid depth. The unknowns of the problem are the Cartesian locations of a fluid particle ($x(a,b,t)$, $z(a,b,t)$) and the fluid pressure $p(a,b,t)$. Thus, the problem is described by the system:

$$\frac{\partial J}{\partial t} = x_{at}z_b + x_a z_{bt} - x_{bt}z_a - x_b z_{at} = 0 \text{ with } J = \frac{\partial(x,z)}{\partial(a,b)} = 1, \tag{A.1a}$$

$$x_{at}x_b - x_a x_{bt} + z_{at}z_b - z_a z_{bt} = 0, \tag{A.1b}$$

$$\frac{\partial \phi}{\partial a} = x_t x_a + z_t z_a \text{ and } \frac{\partial \phi}{\partial b} = x_t x_b + z_t z_b, \tag{A.1c}$$

$$\frac{p}{\rho} = -\frac{\partial \phi}{\partial t} - gz + \frac{1}{2}\left[\left(\frac{\partial x}{\partial t}\right)^2 + \left(\frac{\partial z}{\partial t}\right)^2\right], \tag{A.1d}$$

$$p = 0 \text{ and } b = 0 \tag{A.1e}$$

$$v = z_t = 0 \text{ and } z = b = -d \tag{A.1f}$$

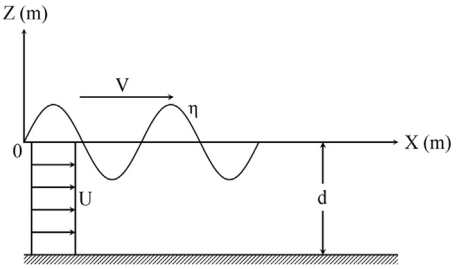


**Fig. A1.** Diagram showing a continuous wave train propagating on a uniform current.

where the indices *a*, *b*, and *t* represent the partial derivatives according to these variables, $\varphi(a,b,t)$ is the velocity potential function in a Lagrangian representation, and *g* is the acceleration of gravity.

A Lagrangian angular frequency, $\sigma$, of fluid particle motions is introduced to avoid the appearance of a secular term. The system is then solved by perturbation theory by introducing a term $\varepsilon$ to identify the order of the related term:

$$x = a + Ut + \sum_{n=1}^{\infty}\varepsilon^n\left[f_n(a,b,\sigma t) + f_n'(a,b,\sigma_0 t)\right], \tag{A.2a}$$

$$z = b + \sum_{n=1}^{\infty}\varepsilon^n\left[g_n(a,b,\sigma t) + g_n'(a,b,\sigma_0 t)\right], \tag{A.2b}$$

$$\phi = Ua + \frac{1}{2}U^2 t + \sum_{n=1}^{\infty}\varepsilon^n\left[\phi_n(a,b,\sigma t) + \phi_n'(a,b,\sigma_0 t)\right], \tag{A.2c}$$

$$p = -\rho g b + \sum_{n=1}^{\infty}\varepsilon^n p_n(a,b,\sigma t), \tag{A.2d}$$

$$\sigma = \sigma_0 ab + \sum_{n=1}^{\infty}\varepsilon^n\sigma_n(a,b) = \frac{2}{\pi}T_L \tag{A.2e}$$

where *U* is the speed of a uniform steady flow, and $\rho$ is the density of the fluid. In these expressions, $f_n$, $g_n$, $\varphi_n$, $p_n$, and $\sigma_n$ are assumed to be associated with the harmonic of order *n*. $f'_n$, $g'_n$, $\varphi'_n$, and $p'_n$ are non-periodic functions that increase linearly with the time *t*. $T_L$ is the period corresponding to the angular frequency. By introducing Eqs. A.2 in the system of Eqs. A.1, Chen et al. (1964, 2012) obtained a series of non-homogeneous differential equations that can be solved successively. The solution of this system for the variables *x*, *z*, and $\sigma$ is then up to the third order. At the first order:

$$f_1 = -\alpha\frac{\cosh(g)}{\cosh(e)}\sin(f), \tag{A.3a}$$

$$g_1 = \alpha\frac{\sinh(g)}{\cosh(e)}\cos(f), \tag{A.3b}$$

$$f_1' = g_1' = 0, \tag{A.3c}$$

$$\sigma_0 = gk\tanh(e), \tag{A.3d}$$

$$e = kd, \tag{A.3e}$$

$$f = ka - \sigma t, \tag{A.3f}$$

$$g = k(b+d) \tag{A.3g}$$

where the parameter $\alpha$ represents the amplitude function of fluid particle motions. The wave amplitude is $a_0 = \alpha\tanh(kd)$ where $k = 2\pi/L$ is the wave number and *L* the wavelength. At the second order:

$$f_2 = -\frac{3}{8}\alpha^2 k\left(\tanh^{-2}(e) - \tanh^2(e)\right)\frac{\cosh(2g)}{\cosh(2e)}\sin(2f) + \frac{1}{4}\alpha^2 k\left(1 - \tanh^2(e)\right)\sin(2f), \tag{A.4a}$$

$$f_2' = \frac{1}{2}\alpha^2 k\left(1 + \tanh^2(e)\right)\frac{\cosh(2g)}{\cosh(2e)}\sigma_0 t \tag{A.4b}$$

$$g_2 = \frac{3}{8}\alpha^2 k\left(\tanh^{-2}(e) - \tanh^2(e)\right)\frac{\sinh(2g)}{\cosh(2e)}\cos(2f) + \frac{1}{4}\alpha^2 k\left(1 + \tanh^2(e)\right)\frac{\sinh(2g)}{\cosh(2e)}, \tag{A.4c}$$

$$g_2' = \sigma_1 = 0. \tag{A.4d}$$

At the third order:

$$f_3 = \left[-\beta_3\frac{\cosh(3g)}{\cosh^3(e)}\frac{1}{12}\alpha k(10\beta_2 - \alpha^2 k)\frac{\cosh(g)}{\cosh^3(e)}\right]\sin(3f)$$

$$-\left[\frac{1}{2}\alpha k(5\beta_2+\alpha^2 k)\frac{\cosh(3g)}{\cosh^3(e)}+\lambda_3\frac{\cosh(g)}{\cosh^3(e)}\right]\sin(f), \tag{A.5a}$$

$$g_3=\left[\beta_3\frac{\sinh(3g)}{\cosh^3(e)}-\frac{1}{2}\alpha k\beta_2\frac{\sinh(g)}{\cosh^3(e)}\right]\cos(3f) -\left[\frac{1}{4}\alpha k(6\beta_2+\alpha^2 k)\frac{\sinh(3g)}{\cosh^3(e)}+\lambda_3\frac{\sinh(g)}{\cosh^3(e)}\right]\cos(f), \tag{A.5b}$$

$$f_3^{'}=g_3^{'}=0, \tag{A.5c}$$

$$\sigma_2=-\frac{1}{2}\alpha^2k^2\sigma_0\frac{\cosh(2g)}{\cosh^2(e)}+\frac{1}{16}\alpha^2k^2\left(9\tanh^{-2}(e)-10+9\tanh^2(e)\right)\sigma_0 \tag{A.5d}$$

where

$$\beta_2=\frac{3}{8}\alpha^2k\left(\tanh^{-2}(e)-1\right), \tag{A.6a}$$

$$\beta_3=\frac{1}{64}\alpha^3k^2\left(9\tanh^{-4}(e)-22\tanh^{-2}(e)+13\right). \tag{A.6b}$$

These equations are used to model the trajectories of suspended particles within the secondary waves of bores. An envelope must, however, be added in order to represent the decay of the amplitude of stubbles. In this study, a simple exponential decay function was chosen.

## References


Auton, T. R., Hunts, J. C., & Prud Homme, M. (1988). The force exerted on a body in inviscid unsteady non-uniform rotational flow. *Journal of Fluid Mechanics*, *197*, 241–257.

Bardina, J., Ferziger, J., & Reynolds, W.C. (1980). Improved subgrid-scale models for large-eddy simulation. In , *Fluid Dynamics and Colocated Conferences, Proceedings of the 13th fluid and plasma dynamics conference*, Snowmass, 10 p.

Barré de Saint Venant, A. (1871). Théorie et équations générales du mouvement non permanent des eaux courantes. *Comptes rendus des Séances de l'Académie des Sciences*, *73*, 147–154 (In French).

Basset, A. B. (1888). On the motion of a sphere in a viscous liquid. *Philosophical Transactions of the Royal Society*, *79*, 43–63.

Bazin, M. H. (1865a). *Rapport aux remous et la propagation des ondes*, Report to the Academy of Sciences, Paris. (In French).

Bazin, M. H. (1865b). Recherches expérimedntales sur la propagation des ondes. *Mémoires présentés par divers savants à l'Académie des Sciences*, *19*, 495–552 (In French).

Bazin, M. H., & Darcy, H. (1865). Recherches expérimentales sur l'écoulement de l'eau dans les canaux découverts. *Mémoires présentés par divers savants à l'Académie des Sciences*, *19*, 1–494 (In French).

Berchet, A. (2014). *Modélisation par des méthodes lagrangiennes du transport sédimentaire induit par les mascarets (Ph.D. dissertation)*. Doctoral School of Science & Engineering of Materials, Mechanics, Energy & Aeronautics, University of Poitiers.

Bessel, F. W. (1826). *Untersuchungen über die Länge des einfachen Sekundenpendels*. Berlin: Konigliche Akademie der Wissenschaften (In German).

Bidone, G. (1825). *Expériences sur la propagation du remous*. Turin: Imprimerie Royale (In French).

Bonneton, N., Bonneton, P., Parisot, J. P., Sottolichio, A., & Detandt, G. (2012). Tidal bore and mascaret - example of Garonne and Seine rivers. *Comptes Rendus Geosciences*, *344*, 508–515.

Bonneton, P., Bonneton, N., Parisot, J. P., & Castelle, B. (2015). Tidal bore dynamics in funnel-shaped estuaries. *Journal of Geophysical Research: Ocean*, *120*, 923–941.

Bonneton, P., Parisot, J.P., Bonneton, N., Sottolichio, A., Castelle, B., Marieu, V., …van de Loock, J. (2011). Large amplitude undular tidal bore propagation in the Garonne River, France. In , *In Proceedings of the 21st international society of offshore and polar engineering (ISOPE) Conference*( pp. 810–814), Maui, Hawai.

Champion, H.H., & Corkan, R.H. (1936). The bore in the Trent. In *Proceedings of the Royal Society of London Series A, mathematical and physical sciences* (pp. 158–181).

Chanson, H. (2010a). Undular tidal bores: Basic theory and free-surface characteristics. *Journal of Hydraulic Engineering*, *136*, 940–944.

Chanson, H. (2010b). Unsteady turbulence in tidal bores: Effects of bed roughness. *Journal of Waterway, Port, Coastal, and Ocean Engineering*, *136*, 247–256.

Chanson, H. (2011). *Tidal bores, aegir, eagre, mascaret, pororoca: Theory and observations*. World Scientific.

Chanson, H. (2012). Momentum considerations in hydraulic jumps and bores. *Journal of Irrigation and Drainage Engineering*, *138*, 382–385.

Chanson, H., & Lubin, P. (2013). Mixing and sediment processes induced by tsunamis propagating upriver In: T. CAI (Ed.), *Tsunamis: Economic impact, disaster management and future challenges* (pp. 65–102). Hauppage, New York: Nova Science Publishers.

Chanson, H., & Tan, K. K. (2011). Dispersion of fish eggs under undular and breaking tidal bores. *Fluid Dynamics and Materials Processing*, *7*, 403.

Chen, Y. Y., & Chen, H. S. (2014). Lagrangian solution for irrotational progressive water waves propagating on a uniform current: Part 1. Fifth-order analysis. *Ocean Engineering*, *88*, 546–567.

Chen, Y. Y., Hsu, H. C., & Chen, G. (2010). Lagrangian experiment and solution for irrotational finite-amplitude progressive gravity waves at uniform depth. *Fluid Dynamics Research*, *42*(4).

Chen, Y. Y., Hsu, H. C., & Hwung, H. (2012). Particle trajectories beneath wave-current interaction in a two-dimensional field. *Nonlinear Processes in Geophysics*, *19*, 185–197.

Chen, Y. Y., Li, M. S., Hsu, H. C., & Ng, C. O. (1964). Theoretical and experimental study of particle trajectories for nonlinear water waves propagating on a sloping bottom. *Philosophical Transactions of the Royal Society A: Mathematical, Physical and Engineering Sciences*, *370*, 1543–1571.

Clift, R., Grace, J. R., & Weber, M. E. (1978). *Bubbles, drops and particles*. Waltham, Massachusetts: Academic Press.

Coates, R. (2007). The genealogy of eagre'tidal surge in the river Trent'. *English Language and Linguistics*, *11*, 507–523.

Davidson, P. (2015). *Turbulence: An introduction for scientists and engineers*. Oxford: University Press.

de Lagrave-Sorbie, M. (1806). Sur le mascaret de la Dordogne. *Journal de Physique, de Chimie, d'Histoire Naturelle et des Arts*, *61*, 286 (In French).

Destriau, G., & Destriau, M. (1951). Le mascaret dans les rivières de Gironde. *Annales des Ponts et Chaussées*, *21*, 609–635 (In French).

Deutsch, E. (1992). Dispersion de particules dans une turbulence homogène isotrope stationnaire calculée par simulation numérique directe des grandes échelles. (Ph.D. dissertation). École Centrale de Lyon, France. (In French).

Falgout, R., Jones, J., & Yang, U. (2006). The design and implementation of HYPRE, a library of parallel high performance preconditioners. In *Lecture notes in computational science and engineering, 51, Numerical solution of partial differential equations on parallel computers* (pp. 267-294). Berlin, Heidelberg: Springer.

Favre, H. (1935). *Étude théorique et expérimentale des ondes de translation dans les canaux découverts*. Paris: Dunod (In French).

Faxen, H. (1922). Der widerstand gegen die bewegung einer starren kugel in einer zähen flüssigkeit, die zwischen zwei parallelen ebenen wänden eingeschlossen ist. *Annalen der Physik*, *373*, 89–119 (In German).

Furgerot, L., Mouazé, D., Tessier, B., Perez, L., Haquin, S., Weill, P., & Crave, A. (2016). Sediment transport induced by tidal bores, An estimation from suspended matter measurements in the Sée River (Mont Saint Michel Bay, northwestern France). *Comptes Rendus Geoscience*, *348*, 432–441.

Gaughan, M. K. (1976). *Prediction of breaker type and measurement of surf-bores on an ocean beach (Ph.D. dissertation)*. School of Oceanography, Oregon State University.

Goda, K. (1979). A multistep technique with implicit difference schemes for calculating two- or three-dimensional cavity flows. *Journal of Computational Physics*, *30*, 76–95.

Hsu, H. C. (2016). Particle trajectories for waves on a linear shear current. *Nonlinear Analysis: Real World Applications*, *14*, 2013–2021.

Kataoka, I. (1986). Local instant formulation of two-phase flow. *International Journal of Multiphase Flow*, *12*, 745–758.

Keevil, C. E., Chanson, H., & Reungoat, D. (2015). Fluid flow and sediment entrainment in the Garonne River bore and tidal bore collision. *Earth Surface Processes and Landforms*, *40*, 1574–1586.

Kjerfve, B., & Ferreira, H. O. (1993). Tidal bores: First ever measurements. Ciência e. *Cultura (Journal of the Brazilian Association for the Advancement of Science)*, *45*, 135–138.

Kolmogorov, A. N. (1961). A refinement of previous hypotheses concerning the local structure of turbulence in a viscous incompressible fluid at high Reynolds number. *Journal of Fluid Mechanics*, *13*(1), 82–85.

Lubin, P., Chanson, H., & Glockner, S. (2010a). Large eddy simulation of turbulence generated by a weak breaking tidal bore. *Environmental Fluid Mechanics*, *10*, 578–602.

Lubin, P., & Glockner, S. (2015). Numerical simulations of three-dimensional plunging breaking waves: Generation and evolution of aerated vortex filaments. *Journal of Fluid Mechanics*, *767*, 364–393.

Lubin, P., Glockner, S., Kimmoun, O., & Branger, H. (2010b). Numerical study of the hydrodynamics of regular waves breaking over a sloping beach. *European Journal of Mechanics B/Fluids*, *30*, 552–564.

Lubin, P., Vincent, S., Abadie, A., & Caltagirone, J. P. (2006). Three-dimensional large eddy simulation of air entrainment under plunging breaking waves. *Coastal Engineering*, *53*(8), 631–655.

MacInnis, G. M. (2012). *Spatio-temporal distribution of eggs and age-0 striped bass (Morone Saxatilis) in the Shubenacadie River estuary (Ph.D. dissertation)*. Halifax, Nova Scotia: Department of Plant and Animal Science, Dalhousie University.

Marques Rosas Fernandes, V. H. M., Kamp, L. P. J., Van Heijst, G. J. F., & Clercx, H. J. H. (2016). Interaction of monopoles, dipoles, and turbulence with a shear flow. *Physics of Fluids*, *28*, 093603.

Maxey, M. R., & Riley, J. J. (1983). Equation of motion for a small rigid sphere in a nonuniform flow. *Physics of Fluids*, *26*, 883–889.
Michaelides, E. E. (1997). The transient equation of motion for particles, bubbles and droplets. *Journal of Fluids Engineering*, *119*, 233–247.
Minier, J.P. (1988). *Construction de la trajectoire d'une particule dans un écoulement turbulent*, Rapport Technique, Électricité de France, Chatou, France (In French).
Partiot, H. (1858). Mémoire sur le mascaret. *Comptes Rendus de l'Académie des Sciences de Paris*, *47*, 651–654 (In French).
Partiot, H. (1861). Mémoire sur le mascaret. *Annales des Ponts et Chaussées, Série*, *4* (*1*), 17–48 (In French).
Poisson, S. D. (1831). Mémoires sur les mouvements simultanés d'un pendule et de l'air environnant. *Mémoires Présentés par Divers Savants à l'Académie des Sciences*, *11*, 521–581 (In French).
Pozorski, J., & Minier, J. P. (1998). On the Lagrangian turbulent dispersion models based on the Langevin equation. *International Journal of Multiphase Flow*, *24*, 913–945.
Rayleigh, L. (1908). Note on tidal bores. In *Proceedings of the Royal Society A: mathematical, physical and engineering sciences* (pp. 448–449).
Reesor, C. M. (2012). *Temporal distribution of Morone Saxatilis eggs and larvae, and Neomysis americana in the Shubenacadie estuary (Ph.D. dissertation)*. Halifax, Nova Scotia: Department of Plant and Animal Science, Dalhousie University.
Reungoat, D., Chanson, H., & Caplain, B. (2012). *Field measurements in the tidal bore of the Garonne River at Arcins (June 2012), Hydraulic Model Report No. CH89/12*. Brisbane, Australia: School of Civil Engineering, The University of Queensland.
Reungoat, D., Chanson, H., & Caplain, B. (2014). Sediment processes and flow reversal in the undular tidal bore of the Garonne River (France). *Environmental Fluid Mechanics*, *14*, 591–616.
Robowtham, F. W. (1964). *The Severn Bore*. Exeter, UK: David and Charles.
Rousseaux, G., Mougenot, J. M., Chatellier, L., David, L., & Calluaud, D. (2016). A novel method to generate tidal-like bores in the laboratory. *European Journal of Mechanics/B*, *55*, 31–38.
Ryabenko, A. A. (1998). Representation of a wave jump and group of translation waves as a combination of a solitary wave and cnoidal waves. *Hydrotechnical Construction*, *32*, 246–252.
Sagaut, P. (Ed.). (2006). *Large eddy simulation for incompressible flows: An introduction* (3rd ed.). Berlin, Heidelberg, New York: Springer-Verlag.
Scott Russell, J. (1845). Report In Proceedings of the fourteenth meeting of the British Association for the Advancement of Science, York, September 1844, Report on waves (pp. 311–390), London: John Murray.
Sentinelles Petitcodiac Riverkeeper (SPR) (2001). *Le Mascaret de la rivière Petitcodiac, 250 ans d'anecdotes*. Archives publiques du Nouveau-Brunswick, CP/POB 300, Moncton, Nouveau-Brunswick, Canada E1C 8K9. (In French).
Simon, B. (2013). *Effects of tidal bores on turbulent mixing: A numerical and physical study in positive surges (Ph.D. dissertation)*. Australia: Doctoral School of Physical Science and Engineering, University of Bordeaux, France / School of Civil Engineering, University of Queensland.
Smagorinsky, J. (1963). General circulation experiments with the primitive equations. *Monthly Weather Review*, *91*, 99–164.
Stoker, J. J. (Ed.). (1957). *Water waves: The mathematical theory with applications*. New York: Interscience Publishers.
Stokes, G. G. (1845). On the theories of the internal friction of fluids in motion, and of the equilibrium and motion of elastic solids. *Transactions of the Cambridge Philosophical Society*, *8*, 287–319.
Tull, K. A. (1997). *Spawning activity of striped bass in a tidal bore river: The Shubenacadie-Stewiacke system, Nova Scotia*. Greenville, North Carolina: Department of Biology, East Carolina University.
Wang, Q., & Squires, K. (1996). Large eddy simulation of particle-laden turbulent channel flow. *Physics of Fluids*, *8*, 1207–1223.
Youngs, D. L. (1982). Time-dependent multi material flow with large fluid distortion In: K. W. Morton, & M. J. Baines (Eds.), *Conference series (Institute of Mathematics and Its Applications), Numerical methods for fluid dynamics*. London, New York: Academic Press.